Geochemistry xxx (xxxx) xxx

Contents lists available at ScienceDirect

Geochemistry

journal homepage: www.elsevier.com/locate/chemer

Isotope diffusion and re-equilibration of copper and evaporation of mercury during weathering of tetrahedrite in an oxidation zone

Juraj Majzlan [a,*], Julia Herrmann [a], Martin Števko [b], Jan G. Wiederhold [c], Marina Lazarov [d], Rastislav Milovský [e]

[a] Institute of Geosciences, Friedrich Schiller University, Burgweg 11, D–07749 Jena, Germany
[b] Earth Science Institute, Slovak Academy of Sciences, Dúbravská cesta 9, P.O. Box 106, 840 05 Bratislava, Slovakia
[c] Environmental Geosciences, C-MESS, University of Vienna, Althanstrasse 14, A-1090 Vienna, Austria
[d] Department of Mineralogy, Leibniz University, Callinstrasse 3, D-30167 Hannover, Germany
[e] Earth Science Institute, Slovak Academy of Sciences, Ďumbierska 1, SK-974 01 Banská Bystrica, Slovakia

ARTICLE INFO

Handling Editor: Weiqiang Li

Keywords:
Copper
Mercury
Isotopes
Oxidation zone
Weathering

ABSTRACT

To understand the mobility of heavy metals during oxidative weathering of sulfides, we investigated weathering processes of tetrahedrite [$(Cu,Fe,Zn,Hg)_{12}(Sb,As)_4S_{13}$] in an oxidation zone with abundant siderite ($FeCO_3$) and baryte ($BaSO_4$) at Rudňany (Slovakia). The focus of this work lied in the isotopic ($\delta^{65}Cu$, $\delta^{202}Hg$, $\delta^{34}S$) variations of the minerals during weathering and the interpretation of such changes. In the studied oxidation zone, Hg-rich tetrahedrite converts *in situ* to pockets of powdery cinnabar (HgS) and an X-ray amorphous mixture rich in Sb, Fe, and Cu that slowly re-crystallizes to Cu-rich tripuhyite ($FeSbO_4$). Copper is mobile and precipitates as malachite [$Cu_2(OH)_2(CO_3)$], azurite [$Cu_3(OH)_2(CO_3)_2$], or less abundant clinoclase [$Cu_3(AsO_4)(OH)_3$]. The isotopic composition ($\delta^{65}Cu$) of tetrahedrite correlates well with the degree of weathering and varies between 0.0 ‰ and −4.0 ‰. This correlation is caused by isotopic changes during dissolution and subsequent rapid equilibration of $\delta^{65}Cu$ values in the tetrahedrite relics. Simple diffusion models showed that equilibration of Cu isotopic values in the tetrahedrite relics proceeds rapidly, on the order of hundreds or thousands of years. Abundant secondary iron oxides draw light Cu isotopes from the aqueous solutions and shift the isotopic composition of malachite and azurite to higher $\delta^{65}Cu$ values as the distance to the primary tetrahedrite increases. Clinoclase and tripuhyite have lower $\delta^{65}Cu$ values and are spatially restricted near to the weathering tetrahedrite. The Hg and S isotopic composition of tetrahedrite is $\delta^{202}Hg = -1.27$ ‰, $\delta^{34}S = -1.89$ ‰, that of the powdery secondary cinnabar is $\delta^{202}Hg = +0.07$ ‰, $\delta^{34}S = -5.50$ ‰. The Hg isotopic difference can be explained by partial reduction of Hg(II) to Hg(0) by siderite and the following evaporation of Hg(0). The S isotopic changes indicate no involvement of biotic reactions in the oxidation zone, probably because of its hostility owing to high concentrations of toxic elements. This work shows that the Cu isotopic composition of the primary sulfides minerals changes during weathering through self-diffusion of Cu in those minerals. This finding is important for the use of Cu isotopes as tracers of geochemical cycling of metals in the environment. Another important finding is the Hg in the oxidation zones evaporates and contributes to the global cycling of this element through atmospheric emission.

1. Introduction

Stable isotope ratios of metals, including those of copper and mercury, have become a valuable geochemical tracer in the last years (Wiederhold, 2015; Moynier et al., 2017). In the research of weathering of ore minerals and ore deposits, they complement more traditional methods, such as mineralogical observations, geochemical modeling, or sequential extractions (Antivachis et al., 2017; Equeenuddin et al., 2017; Drahota et al., 2018; Falteisek et al., 2020). Among the many metals investigated, copper and mercury exhibit a remarkably large range of isotopic variations in natural samples, considering that the relative mass differences between isotopes of an element decreases with increasing atomic mass. For Cu, the documented range is ~27 ‰, for Hg, it is ~20 ‰ (see Fig. 6a in Wiederhold, 2015).

Copper has two stable isotopes (^{63}Cu, ^{65}Cu) whose isotope fractionation has been documented as the result of mineral precipitation

* Corresponding author.
E-mail address: juraj.majzlan@uni-jena.de (J. Majzlan).

https://doi.org/10.1016/j.chemer.2023.126019
Received 1 March 2023; Received in revised form 28 July 2023; Accepted 29 July 2023
Available online 2 August 2023

(Zhu et al., 2000; Pękala et al., 2011; Plumhoff et al., 2021), complexation with organic matter (Bigalke et al., 2010; Ryan et al., 2014), coprecipitation of Cu with minerals (Viers et al., 2018; Roebbert et al., 2018), adsorption to mineral surfaces (Balistrieri et al., 2008; Li et al., 2015) or uptake by living organisms (Pokrovsky et al., 2008; Navarrete et al., 2011; Jouvin et al., 2012). The strongest Cu isotope fractionation is observed when a process includes Cu redox change (Ehrlich et al., 2004; Wall et al., 2011; Pękala et al., 2011; Qi et al., 2019).

Mercury has seven stable isotopes (^{196}Hg, ^{198}Hg, ^{199}Hg, ^{200}Hg, ^{201}Hg, ^{202}Hg, ^{204}Hg) which fractionate during volatilization, adsorption, diffusion, microbial-mediated reactions, and abiotic chemical reactions of the element (Blum et al., 2014; Sun et al., 2016; Blum and Johnson, 2017). The isotopes undergo mass-dependent (MDF) and mass-independent (MIF) fractionation. The largest MDF was observed during calcination of Hg-containing materials, but significant variations in δ^{202}Hg were found also in coal, sediments and soils, various organisms, and ore deposits (Smith et al., 2014). Volatilization accounts for MDF in inorganic, high-temperature natural processes, for example during hydrothermal activity (Smith et al., 2005; Tang et al., 2017). Volatilization induces also MIF (Estrade et al., 2009), just as photochemical reduction (Zheng and Hintelmann, 2009), and dark Hg(II) reduction (Zheng and Hintelmann, 2010). The magnitude of MIF in volatilization processes is much smaller than during photochemical reduction, though. The slope of δ^{202}Hg-Δ^{199}Hg trend for volatilization is 0.1, whereas that for photochemical reduction is −3.5, resulting in much larger Δ^{199}Hg values for the latter process (see Fig. 1 in Blum et al., 2014).

Sulfur has several stable isotopes of which ^{32}S and ^{34}S are routinely measured and their relative abundance reported as δ^{34}S. The isotopes of sulfur are considered to belong to the group of 'traditional' isotopes and much more is known about their fractionation than in the case of metals (e.g., Jensen, 1967; Seal II, 2006). The mechanism that causes the largest fractionation is the redox change involving sulfide-sulfate or other species, possibly enhanced by assimilatory or dissimilatory microbial sulfur reduction (Canfield, 2001). The reduced species (aqueous sulfide or sulfide minerals) will be isotopically distinctly lighter than the reservoir of the oxidized species.

The environmental studies that use Cu or Hg isotopes focus on mining waste, air-borne pollution, or legacies from former industrial sites. Little attention was paid to natural oxidation zones, even though they offer insights in long-term behavior of metals near the Earth's surface. Oxidation zones are a part of weathering profiles of ore deposits that develop over geological time scales. They are of general interest because they reflect the combined influence of tectonics, climate, hydrology, and geomorphology (Alpers and Brimhall, 1988). They are model systems that show how can the recently or currently generated man-made pollution look in far future.

In the weathering profiles, the primary, hypogene ores can be oxidized to secondary, supergene minerals (Alpers and Brimhall, 1988; Brimhall et al., 2005). The main process that facilitates the conversion is oxidation and hydration in contact with atmospheric O_2 and meteoric water. There are, however, also reduction reactions operating at the base of the oxidizing zone, leading to the formation of an enrichment zone. In this zone, elements with high affinity to reduced sulfur (e.g., Hg, Cu, Ag) react to form simple secondary sulfides (e.g., HgS, CuS, Ag_2S). The uppermost part of the oxidation zone, the leach cap, is depleted in most but the least soluble elements by the action of meteoric fluids. The oxidation-reduction reactions operate throughout the weathering profile, from the relatively reducing base up to the leach cap, until a mature stage is reached and the supply of the primary, reduced material was exhausted. The sequence of oxidation-reduction processes leads to distinct Cu isotopic signatures with isotopically lighter secondary sulfides and isotopically heavier secondary oxidic minerals (Asael et al., 2007; Mathur and Fantle, 2015).

In this work, we have investigated isotopic signatures of copper, mercury, and sulfur during oxidative weathering of a complex sulfide, tetrahedrite, from an oxidation zone of the siderite-baryte-tetrahedrite deposit Rudňany in Slovakia. Detailed investigation of mineralogical changes, coupled with chemical composition determination, served to correlate isotopic variations of primary and secondary minerals with the progress of weathering. Simple quantitative models of isotopic diffusion (Cu) or loss via evaporation (Hg) document element mobility during weathering and their introduction into the environment. The goal of this work is a better understanding of oxidation-reduction cycling of metals in the oxidation zone, particularly those parts of this process that cannot be seen in mineralogical changes.

2. Materials and methods

2.1. Sampling

The samples of this study were taken from the north-western segment of the Hrubá vein (geographic coordinates 48.88311° N, 20.69414° E) near the village of Rudňany in Slovakia. Sampling took place over the entire outcrop area. We took 34 grab samples, selected on visual inspection of the material and presence of primary or secondary minerals. All minerals were identified in the field, based on extensive experience of one of the co-authors (M.Š.) at this locality. The deposit Rudňany is of metamorphic-hydrothermal origin (Hurai et al., 2008) and was mined in the past for Fe (siderite), baryte, Cu, Ag, Hg, and other commodities.

2.2. Mineral identification

The grab samples were used to prepare polished and thin sections. All sections were initially examined in transmitted and reflected polarized light. Afterwards, the samples with weak mineralization or samples with redundant mineralogy were not considered anymore. Regions of interest in selected ore and thin sections, identified by optical microscopy, were investigated by energy- and wavelength-dispersive (WDX) electron microprobe (EMP) analyses. The WDX analyses were made with the electron microprobe JEOL JXA-8230 Superprobe (Institute of Geoscience of the University of Jena, Germany). All samples were carbon-coated and measured with an accelerating voltage of 15 kV and 5 nA. The spot size was varied between 1 and 10 μm depending on size and behavior of the minerals of interest. Peak overlap correction was used to avoid peak interference between the lines of As and Sb, S and Co, Fe and Pb as well as Se and Cd. The detection limits, calculated from the peak and background counts, the standards, line and time on peak and background for each element, are given in Table S1.

2.3. Isotopic measurements

For determination of the Cu isotopic composition of the Cu-rich minerals, we used in-situ ultraviolet-femtosecond laser ablation multi-collector inductively coupled plasma mass spectrometry (UV-fsLA-MC-ICP-MS). Selected minerals were analyzed directly from the polished sections used previously for reflected-light microscopy and electron-microprobe measurements. The analyses were performed with the ThermoFinnigan Neptune coupled to a Spectra Physics Solstice™ deep-UV (194 nm) femtosecond laser ablation system (Institute of Mineralogy, Leibniz University Hannover, Germany). The method was developed and tested by Lazarov and Horn (2015) who verified the accuracy of the method with respect to interference effects, laser power, and matrix matching. The laser ablation was performed on polished sections under helium atmosphere and the repetition rate was varied between 2 and 25 Hz due to the differences in the Cu concentration (primary/secondary mineral). Prior to entering the torch, argon was mixed into the sample-out line downstream from the ablation chamber. Sampling lines widths were varied between 30 and 60 μm and lengths depending on the size of the mineral. A washout time of 60 s between the measurements was fulfilled. All values are reported as $\delta^{65}Cu = ([(^{65}Cu/^{63}Cu)_{sample}/(^{65}Cu/^{63}Cu)_{NIST976}] - 1) \times 1000$. All data were

measured with respect to a bracketing in-house standard (Lazarov and Horn, 2015) and recalculated to the NIST976 standard. Overall precision of the measurements was better than 0.1 ‰ (2SD) for δ^{65}Cu. All result of Cu isotope measurements on tetrahedrite, malachite, and azurite are listed in Tables S2 and S3.

For the mercury isotope analysis, the Hg-rich samples (tetrahedrite and cinnabar; the purity of the minerals was controlled by powder X-ray diffraction) were manually separated, powdered and dissolved in aqua regia with these individual steps: 1) Weigh in 50 mg of powdered sample in 50 mL centrifuge tubes. 2) Add 3 mL HNO_3 (69 %), 8 mL HCl (37 %) and 1 mL BrCl (in HCl). 3) Shake the tubes laterally (about 150 rpm) at room temperature for at least 18 h in fume hoods without lids. 4) Add 36 mL H_2O-MQ and gentle mix with lids on. 5) Centrifuge for 15 min at 3500 rpm. 6) Decant the supernatant into syringe. 7) Filtrate with 0.45 μm membrane filter into acid cleaned glass vials with Teflon-coated lid. 8) Store digest solutions in the fridge (4 °C) and keep away from direct sunlight. To produce bromine monochloride (BrCl), see Bloom et al. (2003). As background matrix for extractions, digests, standards and washing solution, we used 1 vol% BrCl solution due to its oxidative power and ability to form stable complexes with oxidized Hg (Bloom et al., 2003). The solution of 2.5 % (*w/v*) $SnCl_2$ in 1 M HCl used for cold vapor introduction was made daily. To measure the mercury concentration in the digests, we used cold vapor atomic fluorescence and absorption spectrometry (Milestone DMA-80 L, Environmental Geosciences, University Vienna, Austria). All samples and standards were diluted to 10 μg L^{-1} Hg prior to Hg isotope analysis using a Nu Plasma II multicollector ICP-MS (Environmental Geosciences, University Vienna, Austria) combined with a Cetac HGX-200 cold vapor introduction system and Tl doping (NIST-997) using a desolvating nebulizer (Aridus II, Cetac). For more information, see Wiederhold et al. (2010) and Grigg et al. (2018). All Hg isotope data are reported relative to NIST-3133 which was used as a bracketing standard. Accuracy and precision were demonstrated by repeated analyses of the in-house standard ETH-Fluka throughout the measurement session. The results are reported as $\delta^{202}Hg = ([(^{202}Hg/^{198}Hg)_{sample}/(^{202}Hg/^{198}Hg)_{standard}] - 1) \times 1000$ and $\Delta^{199}Hg$, that is the deviation of $\delta^{199}Hg$ from the expected value based on mass-dependent fractionation (Blum et al., 2014). The results for ETH-Fluka ($\delta^{202}Hg = -1.46 \pm 0.05$ ‰ and $\Delta^{199}Hg = +0.09 \pm 0.04$ ‰, 2SD, n = 5) were consistent with published data from different laboratories (Table S4, Brocza et al., 2019). As an additional quality control, the reference material NIST-2711 (Montana soil, 6.25 mg kg^{-1} Hg) was digested and measured together with the samples. The Hg recovery of the NIST-2711 digest was 98.6 % and the Hg isotope data ($\delta^{202}Hg = -0.08$ ‰ and $\Delta^{199}Hg = -0.20$ ‰) was in excellent agreement with literature data (Smith et al., 2015; Blum and Johnson, 2017). One of the cinnabar samples (Rud 4.1, Table S4) was processed in triplicate and the consistent results demonstrate that excellent reproducibility was not only achieved for reference materials but also for samples.

Stable sulfur isotopes were measured on mass spectrometer MAT253 coupled with elemental analysis device Flash2000 HT plus (Thermo Scientific) in a continuous-flow mode (Earth Science Institute of the Slovak Academy of Sciences, Banská Bystrica). For each analysis, we used 300–400 μg of material that was manually separated and checked under binocular microscope for purity. Sulfur isotope values were calibrated using international standards IAEA-S2 and IAEA-S3 with +22.70 and − 32.30 ‰ CDT, respectively. All values are reported as $\delta^{34}S = ([(^{34}S/^{32}S)_{sample}/(^{34}S/^{32}S)_{CDT}] - 1) \times 1000$, precision of the $\delta^{34}S$ measurement is ±0.21 ‰.

2.4. Diffusion modeling

Measurements of self-diffusion of copper in sulfides (e.g., chalcopyrite, Chen and Harvey, 1975) showed that the self-diffusion of Cu is fast, by several orders of magnitude faster than that of Fe. Self-diffusion of copper in the $Cu_{2-x}S$ phases (chalcocite, djurleite, etc.) (Cassaignon et al., 1998) or bornite (Berger and Bucur, 1996) is similar in magnitude to that in chalcopyrite. Solid-state diffusion rates are comparable with the rates of dissolution, precipitation, and replacement under low-temperature hydrothermal conditions (Adegoke et al., 2021). Copper mobility in these sulfides was likened to ion mobility in solid-state fast ion conductors (Berger and Bucur, 1996), attesting to the possibility of rapid isotopic equilibration even at low temperatures characteristic for weathering.

The isotopic heterogeneity could be both primary (created during the precipitation of the ores from the hydrothermal fluids) or secondary (created during weathering). Here, we will use simple diffusion models to determine the times necessary to obliterate such heterogeneities.

The primary heterogeneity in ore minerals is often manifested as concentric or oscillatory zonality. Such zonality can be modeled by a square-wave function

$$\begin{aligned} f(x) &= C_{bulk} + C_i \; for \; 0 < x \le L \\ f(x) &= C_{bulk} - C_i \; for \; L < x \le 2L \end{aligned} \quad (1)$$

where C_{bulk} is the average concentration of the element or species of interest and C_i is the deviation from C_{bulk}. This function is periodic with a period of 2*L*. For an analytical solution of the second Fick's equation, this function can be approximated as a sine Fourier series. The concentration *C* as a function of time *t* and distance *x* is then

$$C(x,t) = C_{bulk} + \sum_{n=1,3,5,\ldots}^{\infty} \frac{4C_i}{n\pi} sin\left(\frac{n\pi x}{L}\right) exp\left(-\frac{\pi^2 n^2 Dt}{L^2}\right) \quad (2)$$

where *D* is the temperature-dependent diffusion coefficient, defined as $D = D_0 \exp.(-Q/RT)$, with the adjustable parameters D_0 and *Q* reported by Chen and Harvey (1975).

Primary patchy heterogeneities or secondary heterogeneity, created by oxidative dissolution on the surfaces, can be modeled as an inclusion of a certain composition, confined between –*h* and +*h*, in a matrix of different composition. The corresponding function is

$$\begin{aligned} f(x) &= C_0 \; for \; -h \le x \le +h \\ f(x) &= C_s \; outside \; of \; -h \; to \; +h \end{aligned} \quad (3)$$

Here, the solution for the second Fick's equation is a modified equation from Crank (1975), his eq. 2.15)

$$C(x,t) = C_s + \frac{1}{2}(C_0 - C_s)\left[erf\left(\frac{x+h}{2\sqrt{Dt}}\right) - erf\left(\frac{x-h}{2\sqrt{Dt}}\right)\right] \quad (4)$$

The diffusion coefficients used in our calculation were experimentally determined for chalcopyrite or pyrite (Chen and Harvey, 1975). For comparison, the self-diffusion coefficient for Cu in chalcopyrite at 25 °C is 8.2×10^{-20} $m^2 \cdot s^{-1}$, that for Fe is 6.8×10^{-21} $m^2 \cdot s^{-1}$ and for Fe in pyrite only 1.2×10^{-23} $m^2 \cdot s^{-1}$. The self-diffusion coefficient for sulfur at the same temperature is much lower, 1.3×10^{-37} $m^2 \cdot s^{-1}$. There are no diffusion coefficients for tetrahedrite but it can be assumed that chalcopyrite and tetrahedrite are roughly similar in terms of mobility and self-diffusion of metals.

3. Results

3.1. Primary minerals

The primary mineralization at Rudňany consists mostly of siderite, baryte, sulfides, and minor quartz. Chemical formulae of all minerals mentioned in the text are summarized in Table 1. It has to be pointed out, however, that the oxidation zone studied here contains only relics of those primary minerals. When samples from the deeper parts of the deposits are examined, they show coarse-grained intergrowths of baryte and siderite, with crystals of centimeter to decimeter size. Among the sulfides, complex Cu-Hg-Sb sulfides of the tetrahedrite-tennantite group (variable chemical composition, see below) predominate and are accompanied by minor chalcopyrite and pyrite. The sulfide aggregates may reach locally size of 50 cm. We estimate (visual observations in the

Table 1
Minerals mentioned in text and their nominal formulae.

Primary minerals			
Tetrahedrite	$(Cu,Fe,Zn,Hg)_{12}(Sb,As)_4S_{13}$	Chalcopyrite	$CuFeS_2$
Pyrite	FeS_2	Siderite	$FeCO_3$
Baryte	$BaSO_4$	Quartz	SiO_2
Gersdorffite	NiAsS		

Secondary minerals			
Malachite	$Cu_2(OH)_2CO_3$	Azurite	$Cu_3(OH)_2(CO_3)_2$
Chalcocite	Cu_2S	Clinoclase	$Cu_3(AsO_4)(OH)_3$
Cornwallite	$Cu_5(AsO_4)_2(OH)_4$		
Goethite	FeOOH	Ferrihydrite	$Fe(OH)_3$
		Cinnabar	HgS
Paraschachnerite	(Ag,Hg)	Roméite	$(Ca,Na,\square)_2Sb_2(O,OH)_7$
Tripuhyite	$FeSbO_4$		

field, microscopic observation in reflected polarized light) that 80–90 % of the primary sulfides belonged to tetrahedrite, the rest to chalcopyrite, and pyrite is present only in traces. Primary cinnabar is known from the Rudňany deposit (Cambel and Jarkovský, 1985) but was not found in the material investigated in this study. Liquid mercury, known as a rare primary mineral from Rudňany (Cambel and Jarkovský, 1985), was not found in the outcrop studied. Our EMP analyses identified rare gersdorffite in the samples studied.

Chemical composition of the minerals of the tetrahedrite-tennantite group is highly variable, within individual aggregates (on a scale of micrometers) and in the outcrop (on a scale of decimeters to meters). In most of the analyses, Sb/(Sb + As) ratio (at.%/at.%) is >0.5 (Fig. 1), meaning that the mineral belongs to tetrahedrite. The Fe/(Fe + Zn) is usually >0.8, with very few analyses having this ratio of <0.5. Mercury content is highly variable, ranging from essentially none to almost 18 wt %. Silver content is low, usually <0.1 wt%. Similar analyses of tetrahedrite from the entire Rudňany ore field, either by electron microprobe or wet-chemical methods, were reported by Rojkovič (1977) and Števko et al. (2015).

Chemical composition of pyrite and chalcopyrite is essentially consistent with their nominal formulae. Some of the analyses of pyrite show elevated Ni and Co, up to 3.5 and 1.3 wt%, respectively. There are occasionally small amounts of Cu in pyrite (< 0.7 wt%) while As, Sb or Pb in both minerals are below 0.2 wt%.

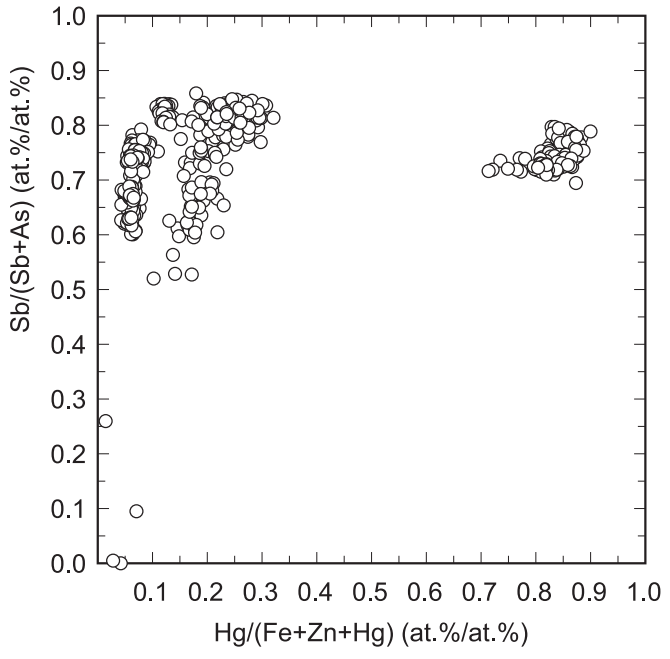

Fig. 1. Atomic elemental ratios in the chemical composition of primary tetrahedrite from Rudňany. All data from EMP analyses.

Chemical composition of the primary carbonates was not investigated in this work because of the omnipresent weathering features. The average composition of the primary hydrothermal carbonates from the Rudňany ore field is $(Fe_{0.818}Mg_{0.127}Mn_{0.048}Ca_{0.007})CO_3$, calculated from the analyses in Cambel and Jarkovský (1985).

3.2. Weathering products

The material in the sampled outcrop is deeply weathered and consists of abundant secondary minerals. Tetrahedrite is replaced *in situ* by compact aggregates of yellowish green color, named trombolite in the early mineralogical literature (e.g., Zepharovich, 1873). For simplicity, we retain this name but emphasize that it is not a mineral. Trombolite is a mixture of X-ray amorphous and poorly crystalline materials.

Weathering of tetrahedrite and chalcopyrite commences along grain boundaries or thin fractures. The thin fractures in tetrahedrite are filled with material rich in Sb, Fe, and Cu (Fig. 2a) and porosity documents loss of material.

In chalcopyrite, these fractures contain secondary copper sulfides, identified in reflected polarized light as chalcocite. Later, even when the relics of the primary sulfides are still present, the secondary copper sulfides in chalcopyrite vanish.

Poorly crystalline materials are common as a weathering product of tetrahedrite. This material, called trombolite, splits into two reservoirs, named veinlets and masses here (Fig. 2b). Veinlets mark the grain boundaries or fractures that started the weathering initially. Masses fill the space enclosed by these veinlets, thus creating a mosaic texture of "grains" of masses, rimmed by the veinlets. In many cases, however, the distinction between the two reservoirs is not clear. Once primary sulfides disappear completely, *trombolite* begins locally to recrystallize and forms aggregates of acicular minerals. Porosity further increases, especially in the masses which are leached and carried away.

Chemical composition of the masses and veinlets is documented by representative analyses in Table 2. Masses accumulate preferentially Cu, As, and Fe. They contain consistently more Hg than the veinlets. Lower totals for the masses show that they contain more volatile components, likely H_2O, perhaps also CO_2. The veinlets store especially Sb; Fe and Cu is comparable to that in the masses, As is distinctly lower. The range of the overall composition of trombolite is graphically shown in Fig. 3. In many cases in Rudňany, the distinction between the masses and veinlets is unclear and trombolite is composed mostly of Sb, Fe, with less Cu and little As.

Copper carbonates are ubiquitous and easy to recognize in the weathered material by macroscopic or microscopic means (Fig. 2c). They are represented by both malachite and azurite. Electron microprobe data identified Cu as the only metal present; hence, the chemical composition of malachite and azurite corresponds to their nominal formulae. There are two modes of occurrence that can be recognized from the textures of the weathered material. Copper carbonates can occur in the vicinity of the weathering primary sulfides, but not directly on them. The other possibility is the occurrence of copper carbonates in cracks further away from the primary sulfides, in the massive and porous accumulations of iron oxides or even on the fractures in country rocks, thus attesting to the mobility of copper during weathering.

Copper arsenates are not as abundant as the carbonates and are represented by the dominant clinoclase and less common cornwallite. Apart from Cu and As, they may contain significant amount of Fe and smaller amount of Sb (Fig. 4). They can be found on the tetrahedrite relics or in their immediate vicinity (not further than a few centimeters from the primary sulfides), or in small cavities in trombolite. Their occurrence is restricted to those aggregates of tetrahedrite-tennantite with higher As/(As + Sb) ratios.

Iron oxides are present in abundance and replace the siderite

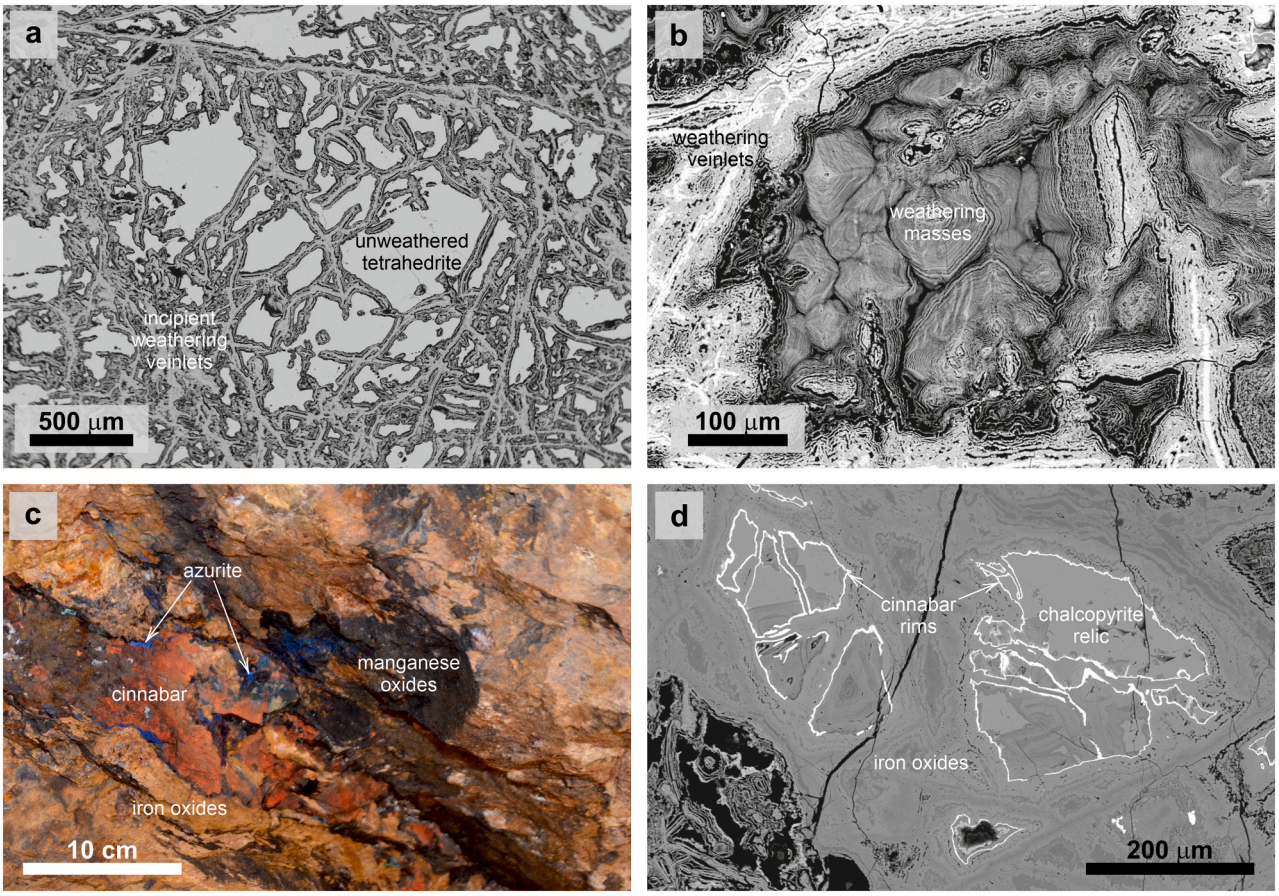

Fig. 2. Back-scattered electron (BSE) images and a photograph of primary and secondary minerals from Rudňany. a) Primary tetrahedrite with incipient weathering veinlets (BSE image); b) Trombolite after complete disappearance of the primary tetrahedrite. The veinlets are rich in Sb and Fe, the masses are rich in Cu and As (BSE image); c) Representative photograph of the oxidation zone with abundant secondary minerals; d) relics of chalcopyrite (ccp) in their weathering products, mostly iron oxides, rimmed by secondary cinnabar.

Table 2
Representative electron microprobe analyses of masses and veinlets from the trombolite with no tetrahedrite relics. All data in weight %. < d.l. = below detection limit.

Material	As_2O_5	Sb_2O_5	SO_3	HgO	Fe_2O_3	ZnO	CuO	Total
Masses	21.20	7.01	1.45	3.81	15.71	< d.l.	21.96	71.14
	21.20	6.74	1.42	3.41	15.96	< d.l.	21.52	70.24
	18.64	6.15	1.82	4.10	14.87	< d.l.	17.41	62.99
Veinlets	7.30	43.75	0.82	1.97	14.44	0.07	17.44	85.79
	11.37	36.91	0.92	2.20	15.47	0.09	20.59	87.55
	6.99	47.08	0.92	2.24	14.71	< d.l.	16.96	88.91

aggregates (Fig. 2c). The phase identified by powder XRD is goethite, but the presence of poorly-crystalline iron oxides, such as ferrihydrite, cannot be excluded. Iron oxides are efficient adsorbers of various components released from the primary minerals. At Rudňany, they contain up to 3.1 wt% SiO_2, 6.0 wt% CuO, 2.4 wt% MnO, and 1.4 wt% As_2O_5. Their Hg content is low, rarely above 0.05 wt%. Typical boxwork textures witness the earlier presence of coarse-grained rhombohedral crystals of siderite. Because of their minor proportions, pyrite and chalcopyrite account only for negligible portion of the iron oxides. They can be identified microscopically as pseudomorphs of the primary sulfides but are overwhelmed by the iron oxides after siderite.

Mercury minerals include the abundant powdery cinnabar (Fig. 2c) and rare microscopic paraschachnerite. Because of its fine-grained nature, cinnabar was difficult to analyze. EMP analyses show elevated Fe and Cu, although it is not clear if these elements actually belong to the cinnabar structure or are found as submicroscopic impurities. Secondary cinnabar is present throughout the profile, always spatially associated with relics of tetrahedrite. Not every aggregate of tetrahedrite is converted to cinnabar, though, because of the pronounced chemical variability of tetrahedrite described above. Obviously, only Hg-rich tetrahedrite released enough Hg to produce the powdery cinnabar masses. In deeper portions of the profile or in large aggregates with unweathered cores, the incipient stages of Hg-tetrahedrite to cinnabar conversion can be observed. The early fractures are filled with dustings of cinnabar that gradually consume the volume of the primary sulfides. Secondary cinnabar may also precipitate on the surfaces of other primary sulfides (Fig. 2d) but this process is of less importance because of the scarcity of these sulfides.

Antimony minerals are seldom even though the tetrahedrite grains contain sufficient amount of Sb. During this work, we detected only a few grains that corresponded chemically to roméite. Tripuhyite has been found on the weathered tetrahedrite aggregates, even as acicular crystals of sizes up to several millimeters. In addition to Fe and Sb, it contains a significant amount of Cu. Textural evidence suggests that

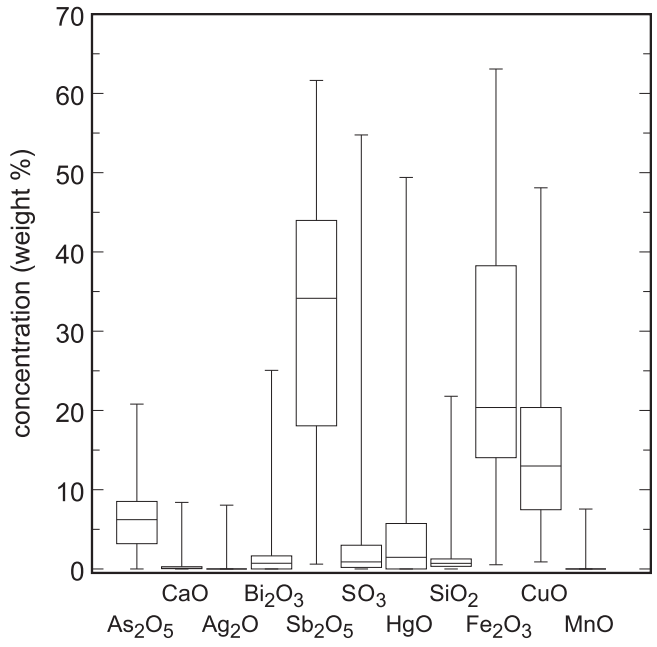

Fig. 3. Ranges of oxide concentrations in trombolite, shown as a series of box-and-whisker diagrams. For each oxide, median is shown by the horizontal line and the 25 and 75 % quartiles by the boxes. The whiskers show the entire range of measured concentrations. All data from EMP analyses.

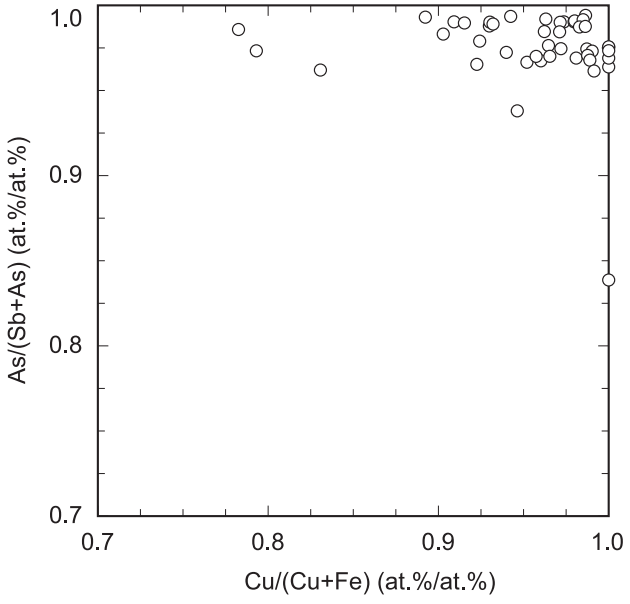

Fig. 4. Atomic elemental ratios in the secondary copper arsenates from Rudňany. All data from EMP analyses.

tripuhyite forms as one of the final products of trombolite transformation.

3.3. Copper isotopes ($\delta^{65}Cu$) in the minerals

Isotopic composition of copper was measured by laser ablation (LA) in all minerals which were large enough to be included in a single LA trace. These include tetrahedrite, chalcopyrite, malachite, azurite, cornwallite, clinoclase, and tripuhyite (the latter contained sufficient Cu for the measurement despite the nominal formula $FeSbO_4$). The secondary copper sulfides and *trombolite* were too small or too porous, respectively, to obtain reliable data. The $\delta^{65}Cu$ values vary from −4 ‰ to nearly +3 ‰ (Fig. 5a).

The most pronounced isotopic variations within one mineral were recorded in tetrahedrite. The measured values from individual LA traces vary from −4.16 to −0.19 ‰. Visual inspection of the BSE images (electronic supporting information) suggested that there may be a relationship between the degree of weathering and the $\delta^{65}Cu$ values. This suggestion was confirmed by image analysis of the same images. The image analysis consisted of manual marking of unweathered and weathered tetrahedrite in the BSE images and counting of the pixels that belonged to each group. Doing so, the proportions of fresh and weathered tetrahedrite in each section were quantified and related to the isotopic composition (Fig. 5b). The data conform to a linear trend with an intercept at −0.35 ‰ that would correspond to the average isotopic composition of fresh tetrahedrite. As the weathering advances, tetrahedrite gets progressively isotopically lighter.

Electron microprobe analyses were carried out next to each LA trace in tetrahedrite. The elemental concentrations changed very little among the individual LA traces and did not correlate with textural changes or with the isotopic data. The variations determined by LA affect only the $\delta^{65}Cu$ values, not the chemical composition of the weathering tetrahedrite.

A similar shift of the $\delta^{65}Cu$ values is seen in chalcopyrite (Fig. 5a) even though a similar quantification is difficult because of fewer analyses and scarcity of this mineral. Strongly weathered chalcopyrite has $\delta^{65}Cu$ values between −3.58 to −1.96 ‰, slightly weathered chalcopyrite values from −1.75 to −0.45 ‰. The division is, however, based only on visual estimate of the weathering progress.

Malachite and azurite are isotopically heavier than the primary sulfides (Fig. 5a). Malachite and azurite in fractures in the vicinity of the primary sulfides have average $\delta^{65}Cu$ of +0.86 ‰ and +0.82 ‰, respectively. Malachite and azurite found further away, as coatings on or aggregates in iron oxides, are isotopically even heavier, with average $\delta^{65}Cu$ of +2.30 ‰ and +2.22 ‰, respectively (Fig. 5a).

Clinoclase is isotopically heterogeneous (Fig. 5a). The cores have higher $\delta^{65}Cu$ values than the rims but the values in the cores among different grains (and the values in the rims) are not comparable. The differences between the cores and the rims are about 0.5–1.0 ‰. One aggregate of tripuhyite crystals measured in this study had $\delta^{65}Cu$ of −0.50 ‰.

3.4. Mercury and sulfur isotopes ($\delta^{202}Hg$, $\Delta^{199}Hg$, $\delta^{34}S$) in the minerals

Mercury and sulfur isotopes were measured from bulk separates of tetrahedrite and secondary cinnabar. The tetrahedrite samples (n = 4) exhibited a very narrow range of Hg isotope signatures with $\delta^{202}Hg$ of −1.22 ‰ to −1.37 ‰ and $\Delta^{199}Hg$ of +0.01 ‰ to +0.08 ‰. In contrast, the secondary cinnabar samples (n = 5) were isotopically distinct with $\delta^{202}Hg$ of −0.04 ‰ to +0.15 ‰ and $\Delta^{199}Hg$ of −0.11 ‰ to 0.00 ‰ (Table S4). The two minerals are clearly separated in the MDF-MIF space (Fig. 6). Tetrahedrite is isotopically lighter (average of $\delta^{202}Hg$ of −1.27 ‰) than the secondary cinnabar (average + 0.07 ‰). There is a difference in the $\Delta^{199}Hg$ between tetrahedrite (average 0.06 ‰) and secondary cinnabar (−0.06 ‰).

Cinnabar and tetrahedrite show $\delta^{34}S$ values with an average of −5.50 ‰ and −1.89 ‰, respectively.

4. Discussion

The progress of weathering can be followed by the mineralogical, chemical, isotopic, and textural changes of the material inside the ore vein. Initially, tetrahedrite releases a portion of the elements from its structure into the surrounding environment but also retains some of them in a transient material with poor crystallinity – trombolite. Trombolite serves as a long-term source of the metals and metalloids but some elements are relatively immobile.

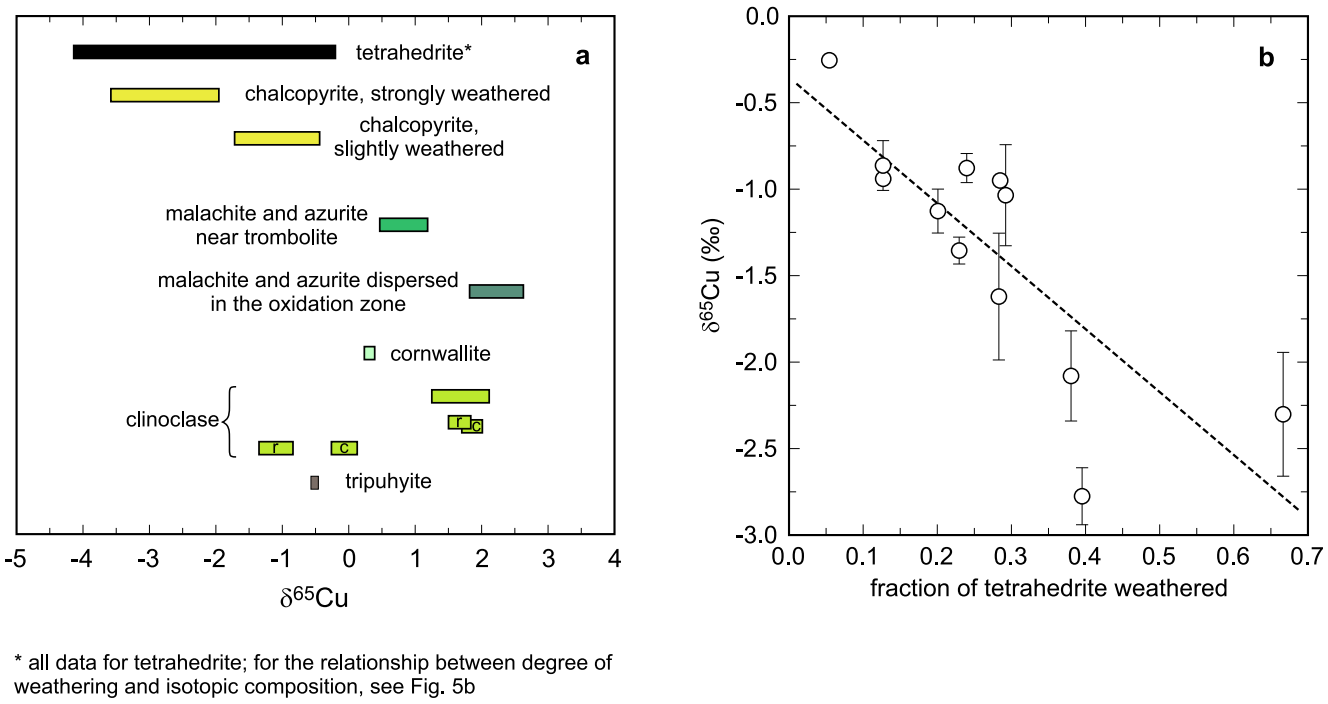

Fig. 5. a) Ranges of δ^{65}Cu values in primary and secondary minerals from the oxidation zone in Rudňany. All data from LA-MC-ICP-MS measurements. r = rim, c = core in the measured clinoclase crystals. b) Isotopic composition of tetrahedrite (measured by LA-ICP-MS) as a function of the fraction of unweathered tetrahedrite (determined by image analysis of BSE images).

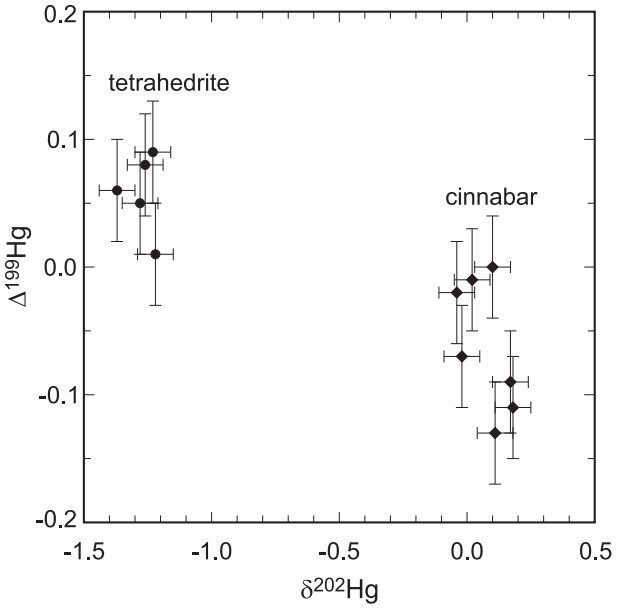

Fig. 6. Mercury isotope differences between the primary tetrahedrite and secondary cinnabar from Rudňany. All data from solution MC-ICP-MS measurements.

Trombolite is a heterogeneous mixture that can split in some cases into two chemically distinct reservoirs, named veinlets and masses, as found in our previous study (Majzlan et al., 2018) and to a limited extent also in Rudňany. In Rudňany, the splitting is not as clear and trombolite is commonly not divided into the two reservoirs. The reason for this observation must be sought in the chemical composition of the primary tetrahedrite. It seems that the element that indicates the development of the two individual reservoirs during weathering is arsenic. Arsenic accumulates in the masses together with Cu (Table 2, see also Majzlan et al., 2018), and is only minor in the Fe-Sb-rich veinlets. However, when As is missing, as in many tetrahedrite aggregates in Rudňany, the two reservoirs do not separate from each other. In As-poor environments, such as those in Rudňany, trombolite is composed of Fe-Sb material with subordinate Cu amount (Fig. 3). Trombolite tends to recrystallize to minute acicular crystals and some of them were identified as Cu-bearing tripuhyite. Hence, the prevailing sink of antimony is the mineral tripuhyite, with variable crystallinity and Cu content.

The main copper sink are the minerals malachite and azurite, dispersed in abundance throughout the oxidation zone. Other secondary Cu minerals are restricted – spatially, temporally and in terms of their abundance. Secondary copper sulfides occur only in chalcopyrite at the beginning of weathering; copper arsenates only on tetrahedrite relics and only when this tetrahedrite is As-enriched; copper oxides only in the deeper portions of the oxidation zone and they are replaced by malachite; copper sulfates are rare and probably mostly recent.

Mercury is scavenged by the abundant powdery cinnabar. It appears that this element is effectively immobilized by sulfide ions released from the primary sulfide minerals. Mercury amalgam (paraschachnerite) is a rare but important witness of the mercury speciation. Amalgamation with mercury can proceed only if Hg^0 is present. Amalgam is rare because its amount is limited by the Ag content in tetrahedrite, which is low in Rudňany. In our previous study (Majzlan et al., 2018), weathered Ag-enriched and Hg-free tetrahedrite contained minute relics of acanthite (Ag_2S). Hence, elements with strong affinity to reduced sulfur, such as Ag or Hg, will be locked in secondary sulfides. Alternatively, weathering-resistant (Hg,Ag) alloys may form, albeit only in small amounts.

4.1. *Changes of isotopic composition of Cu in weathering tetrahedrite*

For the fresh tetrahedrite at the site studied, the δ^{65}Cu value was approximated as −0.35 ‰ (Fig. 5b). During oxidative weathering, the dissolution of tetrahedrite in Rudňany is expected to produce isotopically heavy solution that is the source of copper in the abundant copper carbonates. As a consequence, the surface of tetrahedrite must be

continuously enriched in the light isotopes.

Surface dissolution reactions may produce a similar effect, albeit not always with the same sign, for other minerals. Kinetic effects may lead to preferential dissolution of lighter metal isotopes, e.g., during leaching of goethite (Wiederhold et al., 2006). Dissolution of pyrite leads to isotopically lighter solution (in terms of δ^{56}Fe), but this process was interpreted in terms of equilibrium fractionation (Wolfe et al., 2016). Copper sulfides, on the other hand, appear to behave differently. Chalcopyrite (Kimball et al., 2009; Rodríguez et al., 2015) and bornite (Wall et al., 2011) dissolve to generate isotopically heavier solution. There is a general agreement in the literature that aqueous copper solutions are consistently isotopically heavier after oxidative weathering of Cu sulfides (Fernandez and Borrok, 2009; Kimball et al., 2009; Mathur et al., 2014; Viers et al., 2018).

The range of isotopic shifts determined for dissolution is +2.7 to +3.9 for chalcocite (Mathur et al., 2005; Wall et al., 2010) and +1.5 ‰ to +1.7 ‰ for chalcopyrite (Mathur et al., 2005; Borrok et al., 2008; Kimball et al., 2009). Such isotopic shifts could be expected also for tetrahedrite. Quantification of the isotopic difference between tetrahedrite and the aqueous solutions from our data is difficult because we have no information on the Cu concentrations between the dissolving tetrahedrite and the solution. If the linear trend in Fig. 5b is extrapolated to the final weathering stages (fraction of tetrahedrite consumed approaches 1), then the isotopic composition of the last tetrahedrite remnants would be −4.0 ‰. Then, theoretically, weathering of one primary mineral with a given initial isotopic composition at −0.35 ‰ could account for secondary minerals with a wide range of δ^{65}Cu values. They can start at −4.0 ‰, the isotopic composition of the last tetrahedrite remnant (see Fig. 5b). The upper limit of the range is constrained by the isotopic difference between the dissolving sulfide and the aqueous solution, with the isotopic shifts at the beginning of this paragraph. Hence, the upper limit of this range could lie at +1.0 to +3.0 ‰ of the δ^{65}Cu values. The uncertainty in the upper limit is caused by the variations of the isotopic shifts determined for the dissolution of chalcocite and chalcopyrite (see references above).

4.2. Rates of self-diffusion and isotopic re-equilibration

The correlation between δ^{65}Cu values and degree of weathering (Fig. 5b) necessitates fairly rapid isotopic internal equilibration of the relics of tetrahedrite and chalcopyrite. These relics are separated from each other by secondary products and do not exchange isotopes, except via the fluid phase. At the same time, the relics analyzed by LA-ICP-MS are not perfectly isotopically homogeneous. Hence, one may ask what are the times scales and rates of equilibration and how do they compare to the time scales of weathering in the oxidation zones.

4.3. Age and duration of weathering in oxidation zones

The times scales of re-equilibration, derived from diffusion modeling (below), can be regarded only with respect to the time scales of the natural weathering processes. The earlier data (e.g., Sillitoe and McKee, 1996) agree well with newer U-Pb dating of secondary Cu minerals (Majzlan et al., 2018; Kahou et al., 2021), U–Th–He dating of Fe oxides (Yans et al., 2021), Ar-Ar on Mn oxides (Decrée et al., 2010), or K-Ar on jarosite (Sillitoe, 2019). The ages of oxidation zones reported vary from millions to tens of millions years. The radiometric dating is also supported by geological observations, for example by Miocene lavas overlying already well-developed lateritic profiles (Bowles and Suárez, 2021). There is, however, a difference between the age of an oxidation zone and the duration of weathering. Oxidation zones can be preserved, for example, by tectonic quiescence, glaciation, or burial under volcanic rocks, while the weathering processed ceased. The estimated duration of active weathering is ≈0.5 to 6 Ma (Alpers and Brimhall, 1988; Sillitoe and McKee, 1996; Mathur and Fantle, 2015). These values should be considered when judging the meaning of the diffusion models.

4.4. Simple diffusion models

Diffusion modeling with a square-wave function (eqs. 1, 2) for copper for temperature of 25 °C is graphically displayed in Fig. 7. This function models parallel zones in a mineral and their diffusional homogenization over time. For comparison, diffusion profiles are also shown for Fe self-diffusion. In Fig. 7a, the width of the individual zones is initially 40 μm, a fairly coarse zonality. Most of the Cu isotopic heterogeneity is erased after mere 100 years. The isotopic concentration profile is essentially flat after 300 years. For finer zonality, the homogenization would be even faster. For comparison, the zonality in Fe isotopes in chalcopyrite would be erased after 3000 years in such a model. In pyrite, 1 Ma would be necessary for a similar effect.

Diffusion models for an isolated inclusion in a matrix (Eqs. (3) and (4)) represent grains or relics embedded in their weathering products. Large grains would need more time to homogenize with their surroundings. A 1 mm large grain (Fig. 7b) is larger than what is observed at the site investigated in this work and at most ore deposits in general. After 1000 years (Fig. 7b), Cu isotopic equilibration took place only in the outermost portions of such grain. After 50 ka, homogenization proceeds to an extent that the isotopic difference between the grain and its surroundings is only about a half of the initial difference. Complete homogenization is found after ≈500 ka.

As noted, such large grains are unusual. For smaller grains, homogenization proceeds more quickly. For a grain of 50 μm width, substantial equilibration is seen already after 100 years (Fig. 7c) and almost complete equilibration after ≈1000 years (Fig. 7d). As before, the isotopic equilibration of Fe, either in chalcopyrite or pyrite, is much slower (Fig. 7c, d).

The rapid equilibration can explain why not only the rims of the dissolving copper sulfides, but the entire relics, change continuously their isotopic composition. Shortly after beginning of the weathering, the individual relics are separated from each other. If they exchange isotopes, they may do so only via the aqueous solutions that sustain the oxidative dissolution.

4.5. Copper isotope reservoirs

Strong fractionation of copper isotopes during weathering of ores creates multiple reservoirs with different mineral content and copper isotopic composition. Mathur et al. (2010, 2012) identified such reservoirs in the vertical sections through oxidation, cementation, and primary zones at Cu deposits on the scale of hundreds meters. Asael et al. (2007, 2008) investigated the isotopic fractionation between co-existing secondary sulfides and oxide or silicates. They found that the oxides or oxysalts (such as carbonates or silicates) are consistently isotopically heavier than the sulfides. Mathur and Fantle (2015) found the same trends in a review and model of available data. They linked the Cu isotopic variation in the leach caps and enrichment zones to the global Cu cycle and explained the observed variations by oxidative dissolution of the primary ores and possible reduction of the products at the base of the oxidation zone. Here, we show that such reservoirs and the associated fractionation between mineral pairs (Fig. 5a) develop also on much smaller scales, within a single outcrop.

4.6. Sulfide relics and their immediate vicinity

The most common sulfide is tetrahedrite and it undergoes continuous isotopic re-equilibration during weathering, as discussed above. Its δ^{65}Cu values are becoming progressively lower during this process (Fig. 8a, b). The clinoclase crystals, growing always near the former tetrahedrite, reflect these isotopic changes. They are isotopically zoned, with rims with lower δ^{65}Cu values than the cores (Fig. 5a, 8c). They are receiving the Cu and As directly from the weathering tetrahedrite. The rarer cornwallite and tripuhyite are also isotopically lighter when compared to the much more common copper carbonates. They are also

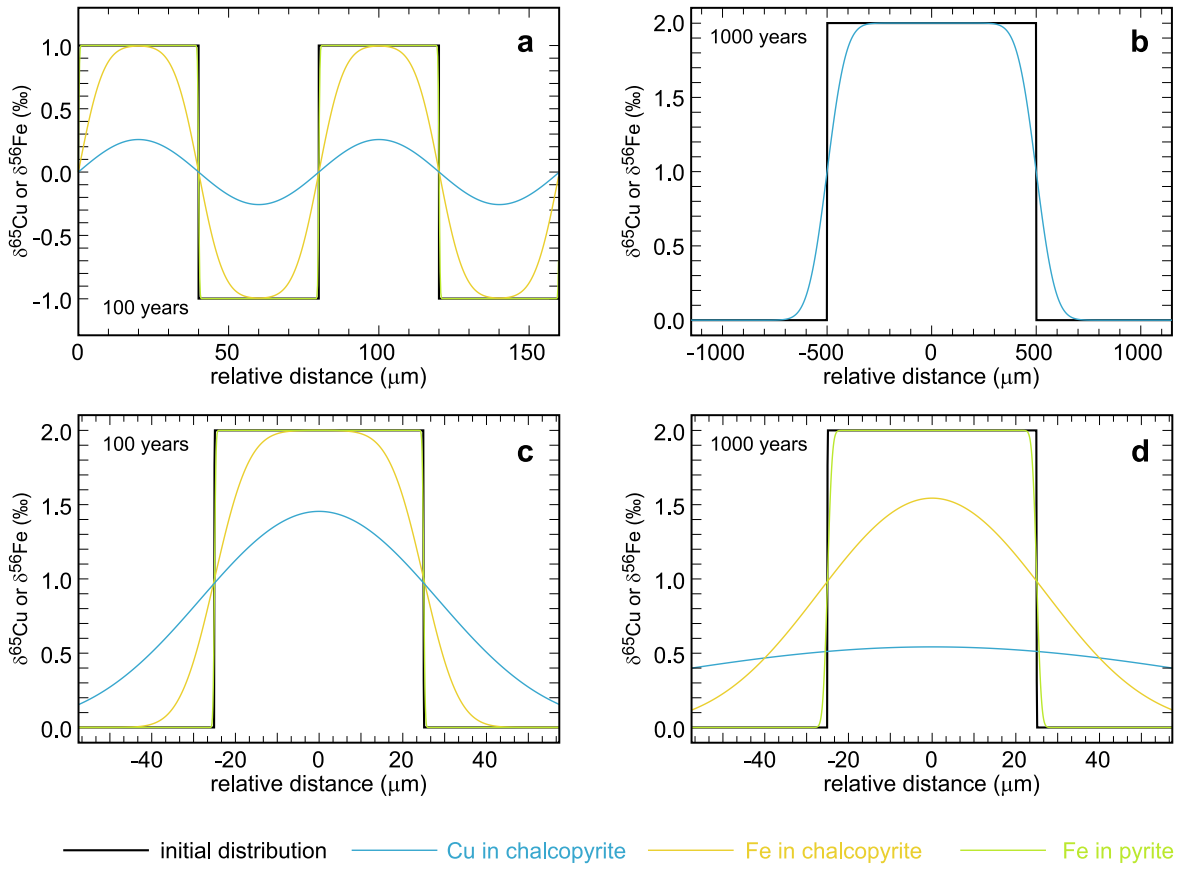

Fig. 7. Results of diffusion calculations for the diffusion of Cu and Fe in chalcopyrite and pyrite. For equations, diffusion coefficients, and details, see text. The time used for the simulation is specified in every panel.

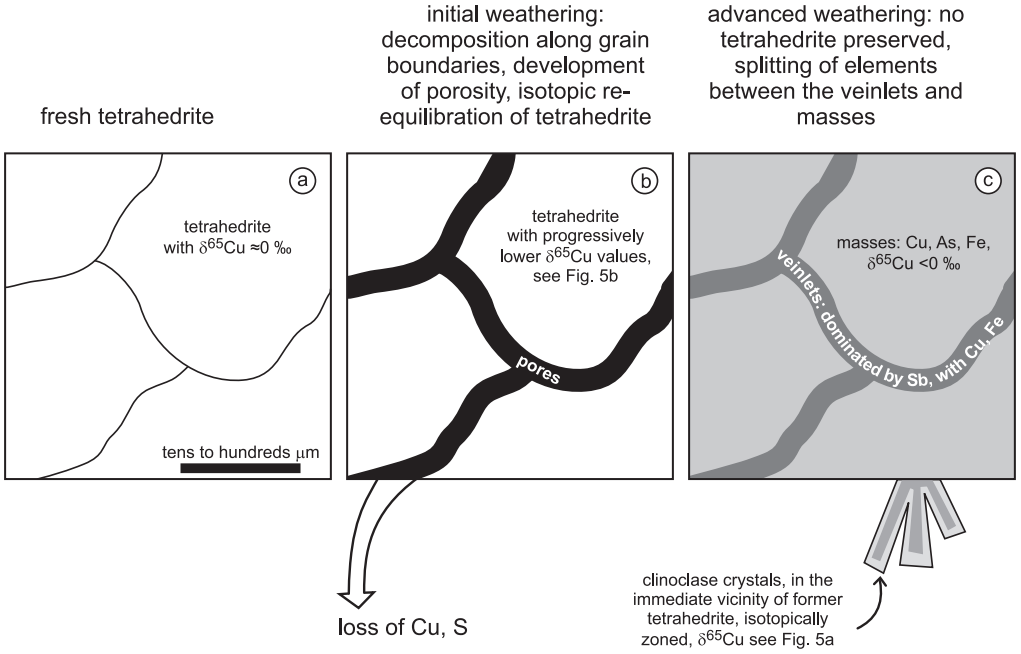

Fig. 8. Sketch and summary of processes, products, and Cu isotopic composition of oxidative weathering of tetrahedrite in the immediate vicinity of the primary sulfides. a) fresh tetrahedrite, b) initial stages of weathering, c) advanced weathering.

spatially restricted to the former tetrahedrite aggregates.

The tetrahedrite aggregates are eventually completely replaced by a mixture of poorly crystalline and X-ray amorphous products that split chemically into the masses and veinlets (Table 2, Fig. 8). The masses and the veinlets contain comparable amount of Cu (Table 2) but the masses are much more voluminous. We assume that they are the primary

carriers of the light Cu isotopes.

4.7. Broader vicinity of the weathering sulfides

Copper is mobile as a divalent ion in the aqueous solutions during weathering. In Rudňany, its mobility is manifested by the presence of malachite and azurite scattered throughout the weathered siderite and in the country rocks (Fig. 9a, b). The copper carbonates are consistently isotopically heavier than the primary tetrahedrite. The fractionation factor for malachite and Cu(II) (Maréchal and Sheppard, 2002; Plumhoff et al., 2021) is small. Therefore, the isotopic composition of malachite (in terms of δ^{65}Cu) reflects closely the isotopic composition of the parental solution. It is likely that such statement can be made also for other secondary oxysalts of Cu(II), including azurite.

A puzzling observation is that the copper carbonates which are further away from the primary tetrahedrite have consistently higher δ^{65}Cu values than those nearby (Fig. 5a, 9b). If this difference would relate only to the isotopic changes in tetrahedrite, then the more distant copper carbonates would have to consistently form from the earliest batches of aqueous solutions derived from tetrahedrite. The mobility of copper, evidenced by the spread of the copper carbonates throughout the oxidation zone, speaks against such possibility. Instead, it is more likely that there is a process that draws the lighter isotopes from the percolating solutions.

A likely sink of the lighter Cu isotopes are the omnipresent iron oxides, especially goethite, produced by weathering of siderite. These iron oxides contain in average 2.1 ± 2.1 wt% CuO (average and standard deviation of 214 EMP analyses). Adsorption of Cu(II) onto iron oxides was reported to lead to preferential incorporation of the light isotopes on the surfaces, with the Δ^{65}Cu (= $\delta^{65}Cu_{adsorbed} - \delta^{65}Cu_{solution}$) of −0.7 to −1.0 ‰ (Pokrovsky et al., 2008; Balistrieri et al., 2008). In agreement with these results, Mathur et al. (2010, 2012) reported very low δ^{65}Cu values, down to −13.5 ‰ for the goethite-hematite dominated leach caps of porphyry-copper deposits. Similarly to iron oxides, manganese oxides are also capable of adsorbing preferentially the light Cu isotopes (e.g., Sherman and Little, 2020). In Rudňany, Mn oxides are subordinate in their amount to the Fe oxides and play probably only a minor role in copper isotope fractionation.

Another mineral that is a potential sink of light copper isotopes is native copper. The data of Qi et al. (2019) show that native copper is isotopically light. Formation of native copper is viable, if considering the reaction.

$$2FeCO_3 + Cu^{2+} + 4H_2O = 2FeOOH + Cu^0 + 2H_2CO_3^0 + 2H^+ \quad (1)$$

At pH = 5, activity of $H_2CO_3^0$ related to the partial pressure of CO_2(g) in the air, and assumed 10 ppm Cu^{2+} in the aqueous solution, the ΔG for this reaction is −71 kJ·mol^{-1} (standard-state data taken from Robie and Hemingway, 1995). In words, aqueous Cu(II) can be reduced by siderite which is widely distributed in Rudňany, to native copper (Cu^0). Native copper was not found microscopically at Rudňany. Abundant nanocrystals of native copper form by reduction of aqueous Cu(II) in delaminated sheet silicates (Fig. 9c). Nanocrystals of native copper were reported from environments related to weathering, in biotite (Ilton and Veblen, 1988), illite (Anh et al., 1997), chlorite (Suárez et al., 2011), or the iron oxide ferrihydrite (Genovese and Mellini, 2007).

The reduction of copper takes place in confined spaces between the delaminated sheets of sheet silicates. Weathering of biotite causes ≈5 % expansion along the 001 basal planes and oxidation of Fe^{2+} (Buss et al., 2008; Goodfellow et al., 2016). It is very likely the oxidation of Fe^{2+} from the structures of the sheet silicates that drives the reduction of copper. Similarly, reduction of copper could occur along cleavage planes of siderite and modify progressively the isotopic composition of aqueous copper pool. This process could operate even in the otherwise oxic environment of the oxidation zone.

In summary, the Cu(II) solutions that percolate through the oxidation zone lose copper (Fig. 9b). Copper loss can be caused by adsorption onto the surface of the ubiquitous iron oxides or reduction to copper nanoparticles. Both processes are capable of drawing lighter isotopes from the aqueous solution (Pokrovsky et al., 2008; Balistrieri et al., 2008; Qi et al., 2019).

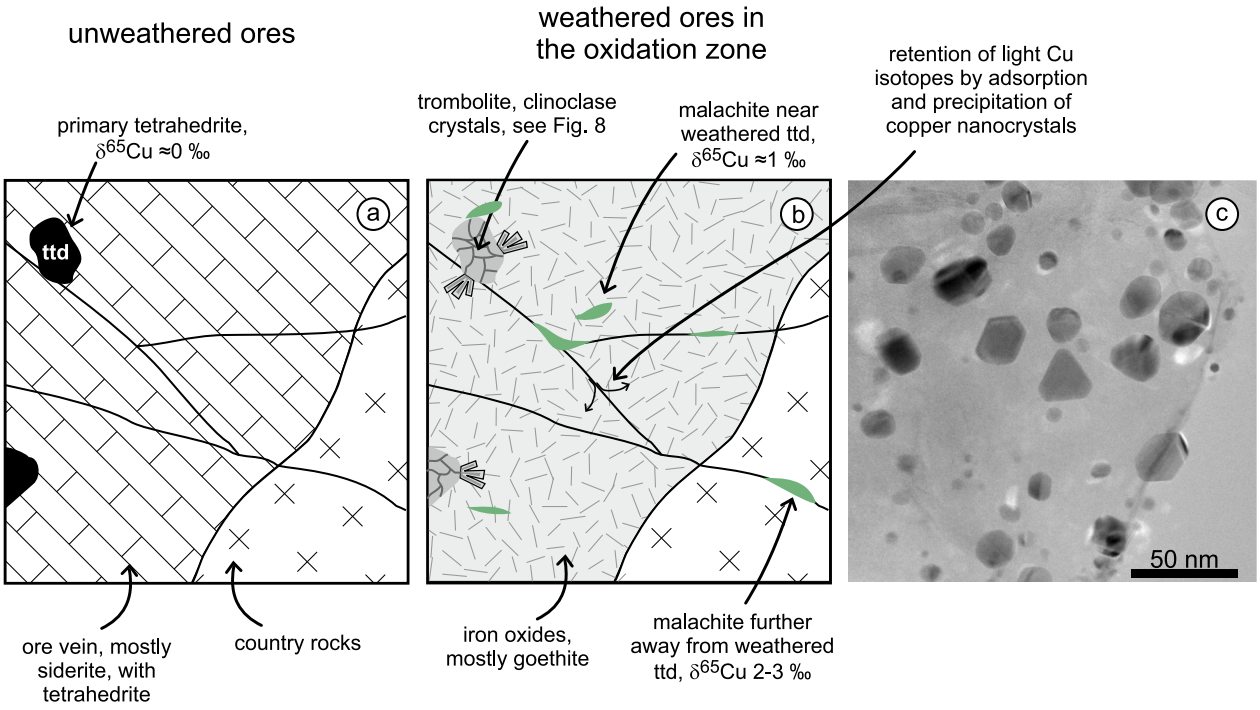

Fig. 9. a,b) Sketch and summary of processes, products, and Cu isotopic composition of oxidative weathering of tetrahedrite in the broader vicinity of the primary sulfides. These processes operate on a scale of meters; the size of the mineral aggregates is exaggerated in the sketches.

4.8. Changes of isotopic composition of Hg during conversion of tetrahedrite to cinnabar

There is a substantial difference in the δ^{202}Hg and Δ^{199}Hg values between the primary tetrahedrite and the secondary cinnabar (Fig. 6). While δ^{202}Hg variations indicate mass-dependent fractionation (MDF), non-zero Δ^{199}Hg values are characteristic for systems which are additionally influenced by mass-independent fractionation (MIF). These can be caused by either magnetic isotope effects or nuclear volume effects and influence mostly the two odd-mass isotopes ^{199}Hg and ^{201}Hg (Wiederhold, 2015). Much about known mechanisms of mercury isotope fractionation was summarized by Blum and Johnson (2017), including microbial methylation, microbial reduction, evaporation, or photochemical reduction. Some of the mechanisms can be readily excluded because the sulfur isotopes (see below) speak clearly against biological contribution during the oxidation weathering at the site studied. One viable fractionation mechanism to explain the observed Hg isotope trends is the evaporation of elemental mercury after partial reduction of Hg(II) from the weathering ores, facilitated by oxidation of the ubiquitous primary siderite (see below). The residue of an evaporation process is expected to be enriched in heavy Hg isotopes (more positive δ^{202}Hg) and exhibit a small negative Δ^{199}Hg shift (e.g., Ghosh et al., 2013). Assuming a simple Rayleigh model for equilibrium fractionation and the fractionation factor from Estrade et al. (2009) (liquid-vapor $\alpha_{202/198} = 1.0067 \pm 0.0011$), approximately 20 % of elemental mercury would have to evaporate to generate the observed isotopic difference (Fig. 10). However, it is necessary to point out that not all mercury was released and could have been converted to Hg^0. Only a portion of Hg(0) evaporated. The remaining Hg(0) could have been re-oxidized and mixed with unfractionated Hg(II) prior to the formation of secondary cinnabar with the observed Hg isotope signature. *Trombolite* is able to retain some mercury, even in the advanced stages of weathering (Fig. 3, Table 2). The heterogeneity of this material, on macro- and microscale, make the quantification of these processes extremely difficult.

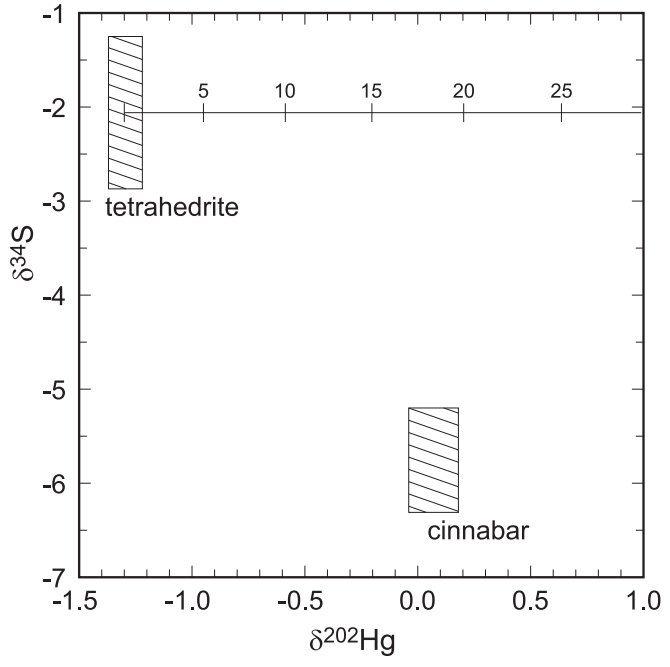

Fig. 10. Isotope differences in mercury and sulfur between primary tetrahedrite and secondary cinnabar from Rudňany. The horizontal line with numbered ticks shows the results of a Rayleigh-model calculation (fractionation data from Estrade et al., 2009) during which liquid mercury evaporates. The starting composition is equal to the average of the measured δ^{202}Hg values for tetrahedrite from Rudňany. The numbers indicate the percentage of mercury evaporated.

Another potential fractionation mechanism to explain the observed Hg isotope trends is the equilibrium isotope fractionation between coexisting Hg(0) and Hg(II) after partial Hg(II) reduction by siderite as recently reported by Wang et al. (2021). For example, based on their fractionation factors, if 45 % of the initial Hg(II) from tetrahedrite was reduced to Hg(0) followed by fast isotope exchange and equilibrium fractionation between the Hg redox states (presumably mediated by the formation of a mercurous dimer as an intermediate species), the Hg(II) pool would be 1.33 ‰ heavier in δ^{202}Hg, corresponding to the observed isotopic difference. In this scenario, the reduced Hg(0) would be completely lost by evaporation and not contribute to the formation of secondary cinnabar. In a similar manner, the observed negative Δ^{199}Hg shift of −0.09 ‰ could be explained by an equilibrium isotope fractionation model with 32 % of total Hg reduced, followed by complete evaporative loss of Hg(0), using the MIF fractionation factor from Wang et al. (2021) indicating a partial influence of the nuclear volume effect to the overall Hg isotope fractionation. Unfortunately, a more detailed quantitative analysis of the observed Hg isotopic difference between primary tetrahedrite and secondary cinnabar is not feasible because the Hg in the two mineral reservoirs cannot be directly linked via a mass balance. However, our isotope data clearly suggest that a significant fraction of Hg must have been lost by evaporation from the weathering zone prior to the formation of secondary cinnabar.

Evaporation of mercury has been observed at former mining sites (Loredo et al., 2005; García-Sánchez et al., 2006) but also over large areas with low mercury concentrations (Gustin et al., 2003). Under arid to semi-arid conditions, evaporation appears to be the main release mechanism of mercury from sites with its higher concentration (Gustin et al., 2003). The mercury flux from non-disturbed mineralized rocks reach hundreds of $ng \cdot m^{-2} \cdot h^{-1}$, but this is only one order of magnitude less than the emissions from sites with mining disturbances. Hence, emissions from a natural source, such as the oxidation zone at Rudňany, can be significant, especially over geological time. They can remove substantial amount of mercury, in agreement with the estimates from the isotopic data. At Rudňany, the main retention option for mercury is its reaction with reduced sulfur and formation of the powdery secondary cinnabar (Fig. 2c).

Mercury, when released from weathering tetrahedrite, could be reduced to the Hg^0 and evaporate. For the reaction.

$$2FeCO_3 + Hg^{2+} + 4H_2O = 2FeOOH + Hg^0 + 2H_2CO_3{}^0 + 2H^+ \quad (2)$$

at pH = 5, activity of $H_2CO_3^0$ related to the partial pressure of CO_2(g) in the air, and assumed 10 mg L^{-1} Hg^{2+} in the aqueous solution, the ΔG for this reaction is −166 $kJ \cdot mol^{-1}$ (standard-state data taken from Robie and Hemingway, 1995). Hence, there is a significant thermodynamic driving force for reduction of Hg(II) to Hg^0 in the presence of siderite.

Reduction of Hg(II) was experimentally documented via oxidation of siderite (eq. 2) (Ha et al., 2017), vivianite (Etique et al., 2021), magnetite (Wiatrovski et al., 2009), or green rust (Remy et al., 2015). In addition, a portion of mercury can be incorporated in the form of submicroscopic inclusions of liquid mercury in primary sulfides, e.g., in pyrite (Manceau et al., 2018). In Rudňany, the most relevant pathway is most likely the reduction of mercury by siderite, an abundant primary mineral in the outcrop studied.

Another potential explanation for the observed isotopic fractionation would be adsorption of Hg(II) onto the ubiquitous iron oxides. A partial sorption of Hg(II) to iron oxides, favoring light Hg isotopes (Jiskra et al., 2012), would create an isotopically heavy remaining aqueous Hg(II) pool, from which the secondary cinnabar may have been formed. Such explanation is, however, not feasible considering the expected Hg reservoir sizes and fractionation factors. The concentration of Hg in the iron oxides in Rudňany is very small (usually <0.05 wt%). Even though the iron oxides are abundant, the secondary cinnabar is also common and holds much more mercury than the iron oxides. Furthermore, the relatively small isotopic fractionation during adsorption of Hg(II) onto

iron oxides of about −0.5 ‰ in δ^{202}Hg (Jiskra et al., 2012) would not be able to generate the observed isotopic difference between tetrahedrite and cinnabar. Thus, even though we cannot completely exclude a minor influence of adsorption processes, our data suggest that evaporation of Hg(0) following partial Hg(II) reduction by siderite was the main fractionation mechanism of Hg isotopes in the studied weathering zone.

4.9. Changes of isotopic composition of S during conversion of tetrahedrite to cinnabar

The isotopic values for the primary tetrahedrite agree well with those determined previously for primary tetrahedrite and chalcopyrite from Rudňany (Žák et al., 1991). The primary cinnabar, not measured in this work, has δ^{34}S values of +3 to +4 ‰ (Žák et al., 1991), much different from those measured for the secondary cinnabar.

The secondary cinnabar is isotopically (δ^{34}S) somewhat lighter than the primary sulfides (Fig. 10). The small difference excludes significant redox contribution (between sulfide and sulfate) or biological action which are known to cause large isotopic shifts for sulfur (e.g., Seal II et al., 2000, p. 562). The isotopic fractionation between H_2S(aq) and sulfides is generally small (Seal II, 2006) and is predicted to be near zero for cinnabar, even at low temperatures (Liu et al., 2014). The small shift between the primary sulfides and secondary cinnabar could be explained by distribution of sulfur isotopes between sulfide and sulfate. Sulfide, released from the weathering sulfides, is oxidized to a small extent to sulfate or transient species of sulfur, and sulfide becomes isotopically lighter.

5. Conclusions

Tetrahedrite, a complex sulfide, undergoes oxidative weathering that produces a variety of minerals and poorly-crystalline materials. The aqueous solutions derived from weathered tetrahedrite can be assumed to have higher δ^{65}Cu values than the sulfide, leaving isotopically lighter tetrahedrite relics behind. Tetrahedrite aggregates fall apart into isolated relics separated from each other by the secondary products. These relics are then in contact with the percolating meteoric water and dissolve over time. Fast copper diffusion homogenizes the tetrahedrite islands on time scales of hundreds to thousands of years, much faster than the estimated lifetime of oxidation zones of 0.5–5.0 Ma. Detectable isotopic heterogeneities in tetrahedrite in Rudňany suggest that the homogenization is continuously disturbed by new batches of aqueous solutions.

The heavy Cu isotopes are stored in the poorly crystalline product trombolite and the minerals which crystallize in the immediate vicinity of the former tetrahedrite. In Rudňany, these include especially the copper arsenates clinoclase and cornwallite, and less common Cu-rich tripuhyite.

Copper carbonates malachite and azurite become isotopically progressively heavier with increasing distance from the weathering tetrahedrite. These isotopic shifts can be assigned to the adsorption of copper onto the ubiquitous iron oxides.

The main finding of this work with respect to Cu isotopes is the fact that the isotopic composition of the weathering primary mineral is continuously adjusting via self-diffusion of copper in that mineral. This fact should be taken into account when using Cu isotopes as an environmental tracer.

The distinct shift in the isotopic composition of mercury can be best explained by evaporation of Hg(0). Reduction of Hg(II) with siderite to Hg(0) is thermodynamically feasible. Simple model calculations with evaporated Hg fractions of between 20 and 45 % are able to explain the isotopic differences between the primary tetrahedrite and the secondary cinnabar, indicating a significant loss of Hg(0) from such weathering zones into the atmosphere. The shift in sulfur isotopes is small and excludes a significant role of biological processes in the metal cycling in the oxidation zone at Rudňany. In summary, natural oxidation zones could contribute substantially to atmospheric emissions of mercury over longer periods of time. Disturbances, such as mining, can accelerate the emission rates.

CRediT authorship contribution statement

J.M.: Conception of the project, field work, image analysis, interpretation of the data, writing, funding acquisition. J.H.: field work, mineral identification, electron microprobe analyses. M.Š.: field work, mineral identification. J.G.W.: Hg isotopic measurements. M.L.: Cu isotopic measurements. R.M.: S isotopic measurements.

Declaration of competing interest

The authors declare that they have no known competing financial interests or personal relationships that could have appeared to influence the work reported in this paper.

Acknowledgements

We are thankful to Ryan Mathur and four anonymous reviewers whose comments improved the quality and clarity of the manuscript. We also appreciate the editorial handling by Astrid Holzheid. This work was financially supported by a *Deutsche Forschungsgemeinschaft* grant MA 3927/19-1.

Appendix A. Supplementary data

The supporting electronic information contains: 1. Table S1: Measurement conditions for the electron microprobe data; 2. Table S2: Electron microprobe data and δ^{65}Cu values for tetrahedrite; 3. Table S3: δ^{65}Cu values for malachite and azurite; 4. Table S4: δ^{202}Hg and Δ^{199}Hg for tetrahedrite and cinnabar; 5. Fig. S1: Twelve back-scattered electron images with positions of EMP analyses and LA traces for the δ^{65}Cu measurements. Supplementary data to this article can be found online at https://doi.org/10.1016/j.chemer.2023.126019.

References

Adegoke, I.A., Xia, F., Deditius, A.P., Pearce, M.A., Roberts, M.P., Brugger, J., 2021. A new mode of mineral replacement reactions involving the synergy between fluid-induced solid-state diffusion and dissolution-reprecipitation: a case study of the replacement of bornite by copper sulfides. Geochim. Cosmochim. Acta. https://doi.org/10.1016/j.gca.2021.04.017.

Alpers, C.N., Brimhall, G.H., 1988. Middle Miocene climatic change in the Atacama Desert, northern Chile: evidence from supergene mineralization at La Escondida. Geol. Soc. Am. Bull. 100, 1640–1656.

Anh, J.H., Xu, H., Buseck, P.R., 1997. Transmission electron microscopy of native copper inclusions in illite. Clay Clay Miner. 45, 295–297.

Antivachis, D.N., Chatzitheodoridis, E., Skarpelis, N., Komnitsas, K., 2017. Secondary sulphate minerals in a Cyprus-type ore deposit, Apliki, Cyprus: mineralogy and its implications regarding the chemistry of pit lake waters. Mine Water Environ. 36, 226–238. https://doi.org/10.1007/s10230-016-0398-0.

Asael, D., Matthews, A., Bar-Matthews, M., Halicz, L., 2007. Copper isotope fractionation in sedimentary copper mineralization (Timna Valley, Israel). Chem. Geol. 243, 238–254.

Asael, D., Matthews, A., Oszczepalski, S., Bar-Matthews, M., Halicz, L., 2008. Fluid speciation controls of low temperature copper isotope fractionation applied to the Kupferschiefer and Timna ore deposits. Chem. Geol. 262, 147–158.

Balistrieri, L.S., Borrok, D.M., Wanty, R.B., Ridley, W.I., 2008. Fractionation of cu and Zn isotopes during adsorption onto amorphous Fe(III) oxyhydroxide: experimental mixing of acid rock drainage and ambient river water. Geochim. Cosmochim. Acta 72, 311–328.

Berger, R., Bucur, R.V., 1996. Diffusion in copper sulphides. An experimental study of chalcocite, chalcopyrite and bornite. In: Swedish Nuclear Power Inspectorate (SKI) Report 96, 3, 35 pages.

Bigalke, M., Weyer, S., Wilcke, W., 2010. Copper isotope fractionation during complexation with insolubilized humic acid. Environ. Sci. Technol. 44, 5496–5502. https://doi.org/10.1021/es1017653.

Bloom, N., Preus, E., Katon, J., Hiltner, M., 2003. Selective extractions to assess the biogeochemically relevant fractionation of inorganic mercury in sediments and soils. Anal. Chim. Acta 479, 233–248.

Blum, J.D., Johnson, M.W., 2017. Recent developments in mercury stable isotope analysis. Rev. Mineral. Geochem. 82, 733–757. https://doi.org/10.2138/rmg.2017.82.17.

Blum, J.D., Sherman, L.S., Johnson, M.W., 2014. Mercury isotopes in earth and environmental sciences. Annu. Rev. Earth Planet. Sci. 42, 249–269.

Borrok, D.M., Nimick, D.A., Wanty, R.B., Ridley, W.I., 2008. Isotopic variations of dissolved copper and zinc in stream waters affected by historical mining. Geochim. Cosmochim. Acta 72, 329–344.

Bowles, J.F.W., Suárez, S., 2021. The formation of alluvial platinum-group minerals: present knowledge and the way ahead. Min. Mag. 85, 12–21. https://doi.org/10.1180/mgm.2021.3.

Brimhall, G., Alpers, C.N., Cunningham, A.B., 2005. Analysis of supergene ore-forming processes and ground-water solute transport using mass balance principles. Econ. Geol. 80, 1227–1256.

Brocza, F.M., Biester, H., Richard, J.-H., Kraemer, S.M., Wiederhold, J.G., 2019. Mercury isotope fractionation in the subsurface of a Hg(II) chloride-contaminated industrial legacy site. Environ. Sci. Technol. 53, 7296–7305. https://doi.org/10.1021/acs.est.9b00619.

Buss, H.L., Sak, P.B., Webb, S.M., Brantley, S.L., 2008. Weathering of the Rio Blanco quartz diorite, Luquillo Mountains, Puerto Rico: coupling oxidation, dissolution, and fracturing. Geochim. Cosmochim. Acta 72, 4488–4507.

Cambel, B., Jarkovský, J., 1985. Rudňany Ore Field: Geochemical and Mineralogical Characteristics. Veda (363 pages. in Slovak).

Canfield, D.E., 2001. Biogeochemistry of sulfur isotopes. Rev. Mineral. Geochem. 43, 607–636.

Cassaignon, S., Pauporté, Th., Guillemoles, J.-F., Vedel, J., 1998. Copper diffusion in copper sulfide: a systematic study. Ionics 4, 364–371.

Chen, J.H., Harvey, W.W., 1975. Cation self-diffusion in chalcopyrite and pyrite. Metall. Trans. B 6, 331–339.

Crank, J., 1975. The Mathematics of Diffusion, Second edition. Clarendon Press. 421 pages.

Decrée, S., Ruffet, G., De Putter, T., Baele, J.-M., Recourt, P., Jamoussi, F., Yans, J., 2010. Mn oxides as efficient traps for metal pollutants in a polyphase low-temperature Pliocene environment: a case study in the Tamra iron mine, Nefza mining district, Tunisia. J. Afr. Earth Sci. 57, 249–261.

Drahota, P., Raus, K., Rychlikova, E., Rohovec, J., 2018. Bioaccessibility of As, Cu, Pb, and Zn in mine waste, urban soil, and road dust in the historical mining village of Kaňk, Czech Republic. Environ. Geochem. Health 40, 1495–1512.

Ehrlich, S., Butler, I., Halicz, L., Rickard, D., Oldroyd, A., Matthews, A., 2004. Experimental study of the copper isotope fractionation between aqueous Cu(II) and covellite, CuS. Chem. Geol. 209, 259–269.

Equeenuddin, S.M., Panda, A., Singh, V., Sahoo, P.K., Sahu, S., Basantray, S.K., 2017. Geochemical appraisal of mine discharge and tailing at Malanjkhand copper mine, India. J. Geol. Soc. India 90, 209–216.

Estrade, N., Carignan, J., Sonke, J.E., Donard, O.F.X., 2009. Mercury isotope fractionation during liquid-vapor evaporation experiments. Geochim. Cosmochim. Acta 73, 2692–2711.

Etique, M., Bouchet, S., Byrne, J.M., ThomasArrigo, L.K., Kaegi, R., Kretzschmar, R., 2021. Mercury reduction by nanoparticulate vivianite. Environ. Sci. Technol. 55, 3399–3407. https://doi.org/10.1021/acs.est.0c05203.

Falteisek, L., Drahota, P., Culka, A., Laufek, F., Trubač, J., 2020. Bioprecipitation of As_4S_4 polymorphs in an abandoned mine adit. Appl. Geochem. 113, 104511 https://doi.org/10.1016/j.apgeochem.2019.104511.

Fernandez, A., Borrok, D.M., 2009. Fractionation of Cu, Fe, and Zn isotopes during the oxidative weathering of sulfide-rich rocks. Chem. Geol. 264, 1–12.

García-Sánchez, A., Contreras, F., Adams, M., Santos, F., 2006. Atmospheric mercury emissions from polluted gold mining areas (Venezuela). Environ. Geochem. Health 28, 529–540.

Genovese, A., Mellini, M., 2007. Ferrihydrite flocs, native copper nanocrystals and spontaneous remediation in the Fosso dei Noni stream, Tuscany, Italy. Appl. Geochem. 22, 1439–1450.

Ghosh, S., Schauble, E.A., Couloume, G.L., Blum, J.D., Bergquist, B.A., 2013. Estimation of nuclear volume dependent fractionation of mercury isotopes in equilibrium liquid–vapor evaporation experiments. Chem. Geol. 336, 5–12.

Goodfellow, B.W., Hilley, G.E., Webb, S.M., Sklar, L.S., Moon, S., Olson, C.A., 2016. The chemical, mechanical, and hydrological evolution of weathering granitoid. J. Geophys. Res. Earth Surf. 121, 1410–1435. https://doi.org/10.1002/2016JF003822.

Grigg, A.R.C., Kretzschmar, R., Gilli, R.S., Wiederhold, J.G., 2018. Mercury isotope signatures of digests and sequential extracts from industrially contaminated soils and sediments. Sci. Total Environ. 636, 1344–1354. https://doi.org/10.1016/j.scitotenv.2018.04.261.

Gustin, M.S., Coolbaugh, M.F., Engle, M.A., Fitzgerald, B.C., Keislar, R.E., Lindberg, S.E., Nacht, D.M., Quashnick, J., Rytuba, J.J., Sladek, C., Zhang, H., Zehner, R.E., 2003. Atmospheric mercury emissions from mine wastes and surrounding geologically enriched terrains. Environ. Geol. 43, 339–351.

Ha, J., Zhao, X., Yu, R., Barkay, T., Yee, N., 2017. Hg(II) reduction by siderite ($FeCO_3$). Appl. Geochem. 78, 211–218.

Hurai, V., Lexa, O., Schulmann, K., Montigny, R., Prochaska, W., Frank, W., Konečný, P., Kráľ, J., Thomas, R., Chovan, M., 2008. Mobilization of ore fluids during Alpine metamorphism: evidence from hydrothermal veins in the Variscan basement of Western Carpathians, Slovakia. Geofluids 8, 181–207.

Ilton, E.S., Veblen, D.R., 1988. Copper inclusions in sheet silicates from porphyry Cu deposits. Nature 334, 516–518.

Jensen, M.L., 1967. Sulfur isotopes and mineral genesis. In: Barnes, H.L. (Ed.), Geochemistry of Hydrothermal Ore Deposits, pp. 143–165.

Jiskra, M., Wiederhold, J.G., Bourdon, B., Kretzschmar, R., 2012. Solution speciation controls mercury isotope fractionation of Hg(II) sorption to goethite. Environ. Sci. Technol. 46, 6654–6662.

Jouvin, D., Weiss, D.J., Mason, T.F.M., Bravin, M.N., Louvat, P., Zhao, F., Ferec, F., Hinsinger, P., Benedetti, M.F., 2012. Stable isotopes of Cu and Zn in higher plants: evidence for Cu reduction at the root surface and two conceptual models for isotopic fractionation processes. Environ. Sci. Technol. 46, 2652–2660. https://doi.org/10.1021/es202587m.

Kahou, Z.S., Brichau, S., Poujol, M., Duchene, S., Campos, E., Leisen, M., d'Abzac, F.-X., Riquelme, R., Carretier, S., 2021. First U-Pb LA-ICP-MS in situ dating of supergene copper mineralization: case study in the Chuquicamata mining district, Atacama Desert, Chile. Mineral. Deposita 56, 239–252. https://doi.org/10.1007/s00126-020-00960-2.

Kimball, B.E., Mathur, R., Dohnalkova, A.C., Wall, A.J., Runkel, R.L., Brantley, S.L., 2009. Copper isotope fractionation in acid mine drainage. Geochim. Cosmochim. Acta 73, 1247–1263. https://doi.org/10.1016/j.gca.2008.11.035.

Lazarov, M., Horn, I., 2015. Matrix and energy effects during in-situ determination of Cu isotope ratios by ultraviolet-femtosecond laser ablation multicollector inductively coupled plasma mass spectrometry. Spectrochim. Acta B 111, 64–73. https://doi.org/10.1016/j.sab.2015.06.013.

Li, D., Liu, S.A., Li, S., 2015. Copper isotope fractionation during adsorption onto kaolinite: experimental approach and applications. Chem. Geol. 396, 74–82.

Liu, S., Li, Y., Tian, H., Yang, J., Liu, J., Shi, Y., 2014. First-principles study of sulfur isotope fractionation in sulfides. Eur. J. Mineral. 26, 717–725.

Loredo, J., Álvarez, R., Ordoñez, A., 2005. Release of toxic metals and metalloids from Los Rueldos mercury mine (Asturias, Spain). Sci. Total Environ. 340, 247–260. https://doi.org/10.1016/j.scitotenv.2004.08.019.

Majzlan, J., Kiefer, S., Herrmann, J., Števko, M., Chovan, M., Lánczos, T., Sejkora, J., Langenhorst, F., Lazarov, M., Gerdes, A., Radková, A., Jamieson, H., Milovský, R., 2018. Synergies in elemental mobility during weathering of tetrahedrite [$(Cu,Fe,Zn)_{12}(Sb,As)_4S_{13}$]: field observations, electron microscopy, isotopes of Cu, C, O, radiometric dating, and water geochemistry. Chem. Geol. 488, 1–20. https://doi.org/10.1016/j.chemgeo.2018.04.021.

Manceau, A., Merkulova, M., Murdzek, M., Batanova, V., Baran, R., Glatzel, P., Saikia, B. K., Paktunc, D., Lefticariu, L., 2018. Chemical forms of mercury in pyrite: implications for predicting mercury releases in acid mine drainage settings. Environ. Sci. Technol. 52, 10286–10296. https://doi.org/10.1021/acs.est.8b02027.

Maréchal, C.N., Sheppard, S.M.F., 2002. Isotopic Fractionation of cu and Zn between Chloride and Nitrate Solutions and Malachite or Smithsonite at 30° and 50 °C (Goldschmidt Conference Abstract Volume).

Mathur, R., Fantle, M.S., 2015. Copper isotopic perspectives on supergene processes: implications for the global Cu cycle. Elements 11, 323–329.

Mathur, R., Ruiz, J., Titley, S., Liermann, L., Buss, H., Brantley, S.L., 2005. Cu isotopic fractionation in the supergene environment with and without bacteria. Geochim. Cosmochim. Acta 69, 5233–5246.

Mathur, R., Dendas, M., Titley, S., Phillips, A., 2010. Patterns in the copper isotope composition of minerals in porphyry copper deposits in southwestern United States. Econ. Geol. 105, 1457–1467.

Mathur, R., Ruiz, J., Casselman, M.J., Megaw, P., van Egmond, R., 2012. Use of Cu isotopes to distinguish primary and secondary Cu mineralization in the Cañariaco Norte porphyry copper deposit, Northern Peru. Mineral. Deposita 47, 755–762. https://doi.org/10.1007/s00126-012-0439-y.

Mathur, R., Munk, L.A., Townley, B., Gou, K.Y., Miguélez, N.G., Titley, S., Chen, G.G., Song, S., Reich, M., Tornos, F., Ruiz, J., 2014. Tracing low-temperature aqueous metal migration in mineralized watersheds with Cu isotope fractionation. Appl. Geochem. 51, 109–115. https://doi.org/10.1016/j.apgeochem.2014.09.019.

Moynier, F., Vance, D., Fujii, T., Savage, P., 2017. The isotope geochemistry of zinc and copper. Rev. Mineral. Geochem. 82, 543–600. https://doi.org/10.2138/rmg.2017.82.13.

Navarrete, J.U., Borrok, D.M., Viveros, M., Ellzey, J.T., 2011. Copper isotope fractionation during surface adsorption and intracellular incorporation by bacteria. Geochim. Cosmochim. Acta 75, 784–799. https://doi.org/10.1016/j.gca.2010.11.011.

Pękala, M., Asael, D., Butler, I.B., Matthews, A., Rickard, D., 2011. Experimental study of Cu isotope fractionation during the reaction of aqueous Cu(II) with Fe(II) sulphides at temperatures between 40 and 200 °C. Chem. Geol. 289, 31–38. https://doi.org/10.1016/j.chemgeo.2011.07.004.

Plumhoff, A.M., Mathur, R., Milovský, R., Majzlan, J., 2021. Fractionation of the copper, oxygen and hydrogen isotopes between malachite and aqueous phase. Geochim. Cosmochim. Acta 300, 246–257. https://doi.org/10.1016/j.gca.2021.02.009.

Pokrovsky, O.S., Viers, J., Emnova, E.E., Kompantseva, E.I., Freydier, R., 2008. Copper isotope fractionation during its interaction with soil and aquatic microorganisms and metal oxy(hydr)oxides: possible structural control. Geochim. Cosmochim. Acta 72, 1742–1757. https://doi.org/10.1016/j.gca.2008.01.018.

Qi, D., Behrens, H., Lazarov, M., Weyer, S., 2019. Cu isotope fractionation during reduction processes in aqueous systems: evidences from electrochemical deposition. Contrib. Mineral. Petrol. 174 https://doi.org/10.1007/s00410-019-1568-4.

Remy, P-Ph., Etique, M., Hazotte, A.A., Sergent, A.-S., Estrade, N., Cloquet, C., Hanna, K., Jorand, F.P.A., 2015. Pseudo-first-order reaction of chemically and biologically formed green rusts with Hg^{II} and $C_{15}H_{15}N_3O_2$: effects of pH and stabilizing agents (phosphate, silicate, polyacrylic acid, and bacterial cells). Water Res. 70, 266–278. https://doi.org/10.1016/j.watres.2014.12.007.

Robie, R.A., Hemingway, B.S., 1995. Thermodynamic properties of minerals and related substances at 298.15 K and 1 bar (10^5 Pascals) pressure and at higher temperatures. U.S. Geol. Survey Bull. 2131 (461 pages).

Rodríguez, N.P., Khoshkhoo, M., Sandström, Å., Rodushkin, I., Alakangas, L., Öhlander, B., 2015. Isotopic signature of Cu and Fe during bioleaching and electrochemical leaching of a chalcopyrite concentrate. Int. J. Miner. Process. 134, 58–65. https://doi.org/10.1016/j.minpro.2014.11.010.

Roebbert, Y., Rabe, K., Lazarov, M., Schuth, S., Schippers, A., Dold, B., Weyer, S., 2018. Fractionation of Fe and Cu isotopes in acidic mine tailings: modification and application of a sequential extraction method. Chem. Geol. 493, 67–79. https://doi.org/10.1016/j.chemgeo.2018.05.026.

Rojkovič, I., 1977. Mineralogical and Geochemical Study on Opaque Minerals of the Rudňany Deposit. Open-File Report. ŠGÚDŠ-Geofond, Bratislava (232 pages. in Slovak).

Ryan, B.M., Kirby, J.K., Degryse, F., Scheiderich, K., McLaughlin, M.J., 2014. Copper isotope fractionation during equilibration with natural and synthetic ligands. Environ. Sci. Technol. 48, 8620–8626. https://doi.org/10.1021/es500764x.

Seal II, R.R., 2006. Sulfur isotope geochemistry of sulfide minerals. Rev. Mineral. Geochem. 61, 633–677. https://doi.org/10.2138/rmg.2006.61.12.

Seal II, R.R., Alpers, C.N., Rye, R.O., 2000. Stable isotope systematics of sulfate minerals. Rev. Mineral. 40, 541–602. https://doi.org/10.2138/rmg.2000.40.12.

Sherman, D.M., Little, S.H., 2020. Isotopic disequilibrium of Cu in marine ferromanganese crusts: evidence from *ab initio* predictions of Cu isotope fractionation on sorption to birnessite. Earth Planet. Sci. Lett. 549, 116540 https://doi.org/10.1016/j.epsl.2020.116540.

Sillitoe, R., 2019. Supergene oxidation of epithermal gold-silver mineralization in the Deseado massif, Patagonia, Argentina: response to subduction of the Chile Ridge. Mineral. Deposita 54, 381–394. https://doi.org/10.1007/s00126-018-0814-4.

Sillitoe, R.H., McKee, E.H., 1996. Age of supergene oxidation and enrichment in the Chilean porphyry copper province. Econ. Geol. 91, 164–179.

Smith, C.N., Kesler, S.E., Klaue, B., Blum, J.D., 2005. Mercury isotope fractionation in fossil hydrothermal systems. Geology 33, 825–828.

Smith, R.S., Wiederhold, J.G., Jew, A.D., Brown Jr., G.E., Bourdon, B., Kretzschmar, R., 2014. Small-scale studies of roasted ore waste reveal extreme ranges of stable mercury isotope signatures. Geochim. Cosmochim. Acta 137, 1–17.

Smith, R.S., Wiederhold, J.G., Jew, A.D., Brown Jr., G.E., Bourdon, B., Kretzschmar, R., 2015. Stable Hg isotope signatures in creek sediments impacted by a former Hg mine. Environ. Sci. Technol. 49, 767–776. https://doi.org/10.1021/es503442p.

Števko, M., Sejkora, J., Peterec, D., 2015. Grumiplucite from the Rudňany deposit, Slovakia: a second world-occurrence and new data. J. Geosci. 60, 269–281.

Suárez, S., Nieto, F., Velasco, F., Martín, F.J., 2011. Serpentine and chlorite as effective Ni-Cu sinks during weathering of the Aguablanca sulphide deposit (SW Spain). TEM evidence for metal-retention mechanisms in sheet silicates. Eur. J. Mineral. 23, 179–196.

Sun, R., Streets, D.G., Horowitz, H.M., Amos, H.M., Liu, G., Perrot, V., Toutain, J.-P., Hintelmann, H., Sunderland, E.M., Sonke, J.E., 2016. Historical (1850-2010) mercury stable isotope inventory from anthropogenic sources to the atmosphere. Elem. Sci. Anth. 4, 000091 https://doi.org/10.12952/journal.elementa.000091.

Tang, Y., Bi, X., Yin, R., Feng, X., Hu, R., 2017. Concentrations and isotopic variability of mercury in sulfide minerals from the Jinding Zn-Pb deposit, Southwest China. Ore Geol. Rev. 90, 958–969.

Viers, J., Grande, J.A., Zouiten, C., Freydier, R., Masbou, J., Valente, T., de la Torre, M.-L., Distrigneville, C., Pokrovsky, O.S., 2018. Are Cu isotopes a useful tool to trace metal sources and processes in acid mine drainage (AMD) context? Chemosphere 193, 1071–1079. https://doi.org/10.1016/j.chemosphere.2017.11.133.

Wall, A., Heaney, P., Mathur, R., Gammons, C., Brantley, S., 2010. Cu isotope systematics of the Butte Mining District, Montana. Geochim. Cosmochim. Acta A1093.

Wall, A.J., Mathur, R., Post, J.E., Heaney, P.J., 2011. Cu isotope fractionation during bornite dissolution: an in-situ X-ray diffraction analysis. Ore Geol. Rev. 42, 62–70. https://doi.org/10.1016/j.oregeorev.2011.01.001.

Wang, Y., Bartov, G., Wang, T., Reinfelder, J.R., Johnson, T.M., Yee, N., 2021. Rapid attainment of isotopic equilibrium after mercury reduction by ferrous iron minerals and isotopic exchange between Hg(II) and Hg(0). ACS Earth Space Chem. 5, 1384–1394. https://doi.org/10.1021/acsearthspacechem.1c00026.

Wiatrovski, H.A., Das, S., Kukkadapu, R., Ilton, E.S., Barkay, T., Yee, N., 2009. Reduction of Hg(II) to Hg(0) by magnetite. Environ. Sci. Technol. 43, 5307–5313. https://doi.org/10.1021/es9003608.

Wiederhold, J., 2015. Metal stable isotope signatures as tracers in environmental geochemistry. Environ. Sci. Technol. 49, 2606–2624. https://doi.org/10.1021/es504683e.

Wiederhold, J.G., Kraemer, S.M., Teutsch, N., Borer, P.M., Halliday, A.N., Kretzschmar, R., 2006. Iron isotope fractionation during proton-promoted, ligand-controlled, and reductive dissolution of goethite. Environ. Sci. Technol. 40, 3787–3793. https://doi.org/10.1021/es052228y.

Wiederhold, J.G., Cramer, C.J., Daniel, K., Infante, I., Bourdon, B., Kretzschmar, R., 2010. Equilibrium mercury isotope fractionation between dissolved Hg(II) species and thiol-bound Hg. Environ. Sci. Technol. 44, 4191–4197. https://doi.org/10.1021/es100205t.

Wolfe, A.L., Stewart, B.W., Capo, R.C., Liu, R., Dzombak, D.A., Gordon, G.W., Anbar, A. D., 2016. Iron isotope investigation of hydrothermal and sedimentary pyrite and their aqueous dissolution products. Chem. Geol. 427, 73–82. https://doi.org/10.1016/j.chemgeo.2016.02.015.

Yans, J., Verhaert, M., Gautheron, C., Antoine, P.-O., Moussi, B., Dekoninck, A., Decrée, S., Chafte, H.-R., Hatira, N., Dupuis, C., Pinna-Jamme, R., Jamoussi, F., 2021. (U-Th)/He dating of supergene iron (oxyhydr-) oxides of the Nefza-Sejnane district (Tunisia): new insights into mineralization and mammalian biostratigraphy. Minerals 11, 260. https://doi.org/10.3390/min11030260.

Žák, K., Radvanec, M., Grecula, P., Bartalský, B., 1991. Sr, S, C, O isotopes and metamorphic-hydrothermal model of vein mineralization in the Gemericum. Miner. Slovaca 23, 95–108 (in Slovak).

Zepharovich, V.V., 1873. Mineralogisches Lexikon für das Kaiserthum Österreich. II. Band. Wilhelm Braumüller, Wien.

Zheng, W., Hintelmann, H., 2009. Mercury isotope fractionation during photoreduction in natural water is controlled by its Hg/DOC ratio. Geochim. Cosmochim. Acta 73, 6704–6715.

Zheng, W., Hintelmann, H., 2010. Nuclear field shift effect in isotope fractionation of mercury during abiotic reduction in the absence of light. J. Phys. Chem. A 114, 4238–4245.

Zhu, X.K., O'Nions, R.K., Guo, Y., Belshaw, N.S., Rickard, D., 2000. Determination of natural Cu-isotope variation by plasma-source mass spectrometry: implications for use as geochemical tracers. Chem. Geol. 163, 139–149.